National Aeronautics and Space Administration

The Origin of Mars' Massive CO_2 Ice Deposit

Author: Peter Buhler (3222)

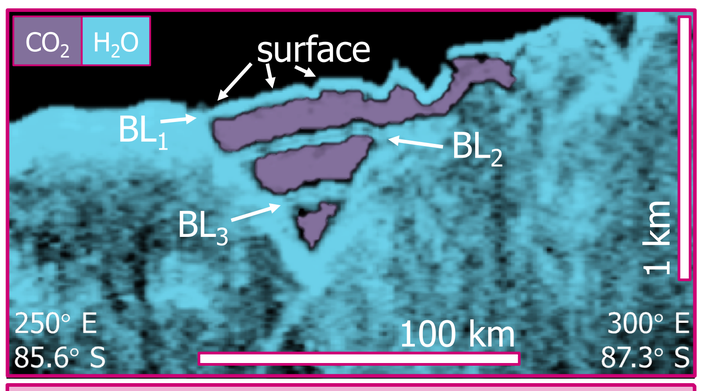
Sylvain Piqueux (3222), Andrew Ingersoll (Caltech), Bethany Ehlmann (3220; Caltech), Paul Hayne (CU Boulder)

What is Mars' Massive CO_2 Ice Deposit (MCID) ?

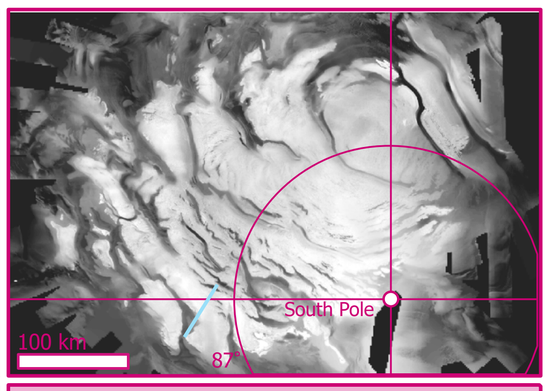
- A CO_2 deposit up to 1 km thick, discovered at Mars' south pole with radar in 2011
- Sits atop the more massive, several-km-thick southern H_2O ice cap
- Overlain by ~20 m H_2O ice, with two more embedded H_2O bounding layers (BLs)
- Above the topmost H_2O ice layer lies 1-10 m of CO_2 ice, called the Residual South Polar Cap (RSPC)

Why is Mars' MCID important?

- Mars' atmosphere is 96% CO_2 by mass
- If released to the atmosphere, the MCID would double Mars' Pressure, significantly affecting Mars' climate and liquid surface H_2O stability



False-color radargram of the MCID



RSPC image mosaic. Blue line: radar trace.

Three outstanding mysteries of Mars' CO_2 ice

- **How was the MCID emplaced with its observed stratigraphy?**
  - *No complete, quantitative models of the MCID's origin and evolution exist*
- **Why does the RSPC exist?**
  - *No explanation; thought to result from special climate event of disputed nature*
- **Why is the MCID only at the south (not north) pole?**
  - *South pole at ~5 km higher elevation, higher elevation disfavors CO_2 stability*

Methods: determine atmosphere-MCID historical evolution

1 For a given orbit

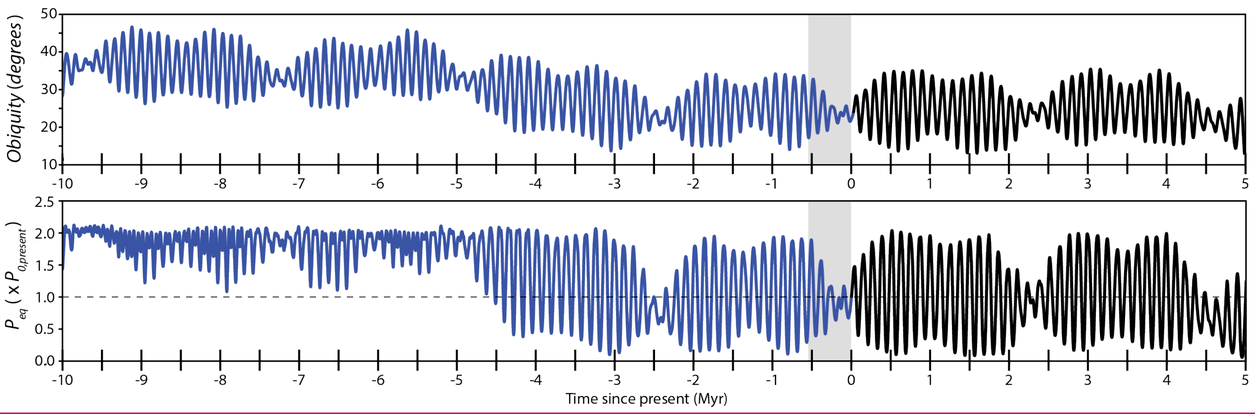
2 CO_2 ice — Mean Annual Equilibrium CO_2 Temperature

3 CO_2 gas, CO_2 ice — Mean Annual Equilibrium Pressure

We Model the co-evolution of MCID and atmosphere mass over Mars' orbital history with a 1-D energy balance model.

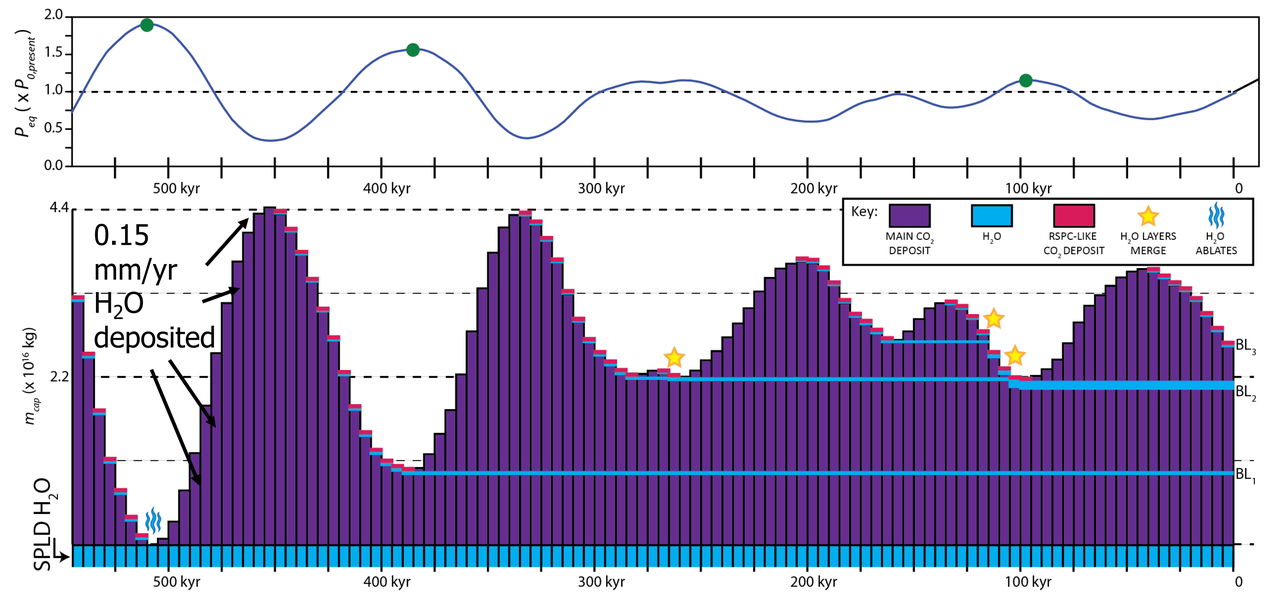
- For various orbits (obliquity, eccentricity, longitude of perihelion):
- Calculate MCID surface CO_2 temperature T_{eq} such that mean annual absorbed insolation flux equals mean annual emitted thermal flux
- T_{eq} depends on the properties (albedo, emissivity) and environment (latitude, atmospheric opacity) of the CO_2 deposit.
- T_{eq} determines mean annual equilibrium pressure P_{eq} from CO_2 phase curve
- MCID always in vapor contact with atmosphere, not sequestered by H_2O layers *This differs from previous models [1,2].*

Results: obliquity drives atmosphere-MCID CO_2 exchange



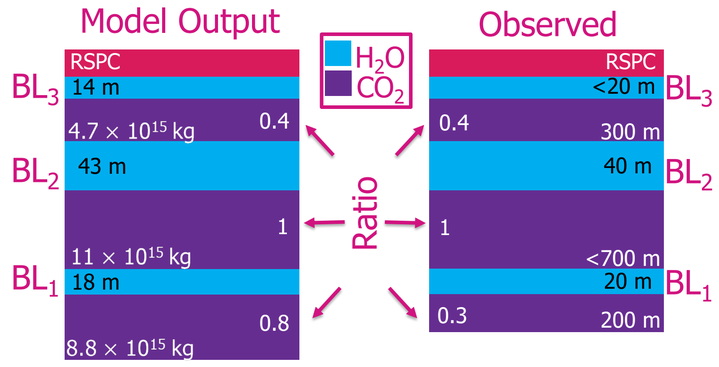
Above: Mars' obliquity history [3] and our model-output pressure history
Low obliquity means Mars' poles point less directly at the sun and cool down, so CO_2 deposits from the atmosphere onto the MCID, lowering the pressure. When obliquity increases, the MCID receives more sunlight and CO_2 returns to the atmosphere.

Results: obliquity sets MCID stratigraphy



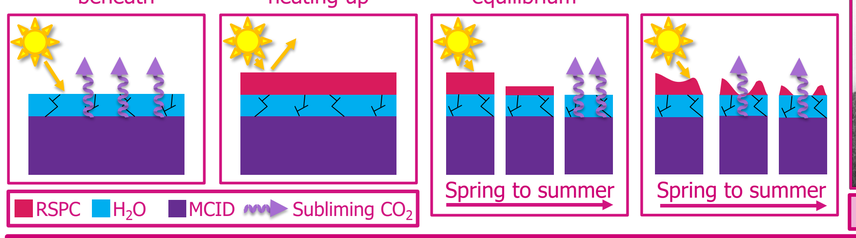
Above: zoom on past 600 kyr of Mars' pressure and MCID mass history
At low obliquity, CO_2 deposits from the atmosphere onto the MCID, and vice versa. H_2O is also cold-trapped onto the MCID at ~0.15 mm/yr [4], resulting in a CO_2 deposit with ~1% impurities. We propose that, when CO_2 ablates, H_2O is left behind as residual lag, which consolidates into the H_2O bounding layers (BLs) seen in radar. When all the CO_2 between two H_2O layers ablates, the H_2O layers merge. H_2O lag layers are buried by CO_2 deposited at subsequent low obliquity periods.

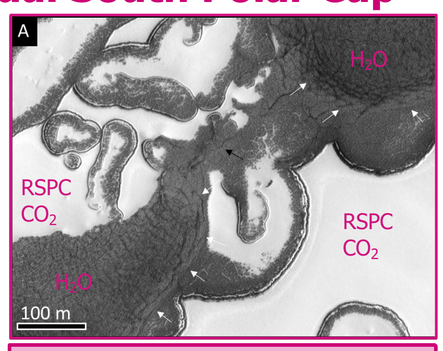
Results: our model output compares well with observation



Our model outputs a mass ratio of CO_2 layers that matches well to the observed ratio of mean CO_2 layer thicknesses [1]. The ratio of H_2O layer thicknesses also matches well. Comparison with the bottom layer is complicated because the ground beneath the MCID is not flat, but we use a 1D model.

Results: our model predicts the Residual South Polar Cap





H_2O ice exposed below RSPC in summer

When top H_2O layer is exposed (through holes in the RSPC), annual solar flux exceeds emitted thermal flux, which heats the H_2O and causes CO_2 to sublime from the MCID beneath the H_2O. Equilibration of H_2O exposure is self-regulating. If the extent and/or duration of H_2O exposure is high then CO_2 sublimation is high and the excess pressure leads to increased persistence of RSPC CO_2 (covering the H_2O) and vice versa. Thus, the RSPC can neither grow large nor completely disappear.

Major Findings

- **How was the MCID emplaced with its observed stratigraphy?** *Orbital forcing drives MCID-atmosphere co-evolution. H_2O impurities form lag deposits.*
- **Why does the RSPC exist?** *Convergent feedback between surface CO_2 ablation, H_2O exposure, basal CO_2 sublimation, and CO_2 surface re-deposition.*
- **Why is the MCID only at the south (not north) pole?** *The albedo/emissivity of south CO_2 is higher than north CO_2, which overwhelms elevation effects.*

Future work

How do the H_2O layers affect the CO_2 cycle?
Previous work suggested that the H_2O seals in the CO_2 [1,2], whereas our model suggests continuous MCID-atmosphere vapor contact. These two hypotheses predict different atmospheric pressure histories. More observation of the H_2O beneath the RSPC is needed to distinguish between them.

National Aeronautics and Space Administration
Jet Propulsion Laboratory
California Institute of Technology
Pasadena, California

www.nasa.gov

Copyright 2019. All rights reserved.

References: [1] Bierson et al. (2016) *GRL* 43, 4172-4179 [2] Manning et al. (2019) *Icarus* 317, 509-517 [3] Laskar et al. (2004) *Icarus* 170, 343-364 [4] Brown et al. (2014) *EPSL* 406, 102-109

Poster No. P-01

National Aeronautics and Space Administration

Mapping VIMS specular reflections on Titan's surface during the Cassini mission

Benoît Seignovert (3222), Kenneth J. Lawrence (3224), Christophe Sotin (4000) and Robert A. West (3222)

Introduction

Besides the Earth, Titan, the largest moon of Saturn, is the only body of the solar system with a dense atmosphere and lakes and seas at its surface. In 2009, during the T58 flyby, the *Visual and Infrared Mapping Spectrometer* (VIMS), onboard the Cassini orbiter, recorded 4 spectral cubes containing a very unusual signature presenting a very high *I/F* infrared peak around 5 µm in a specular geometry [1]. This observation, located on a radar smooth area [2] is the first confirmation of the presence of large hydrocarbon liquids in Titan's North Pole.

Between 2010 and 2014, a dozen of new specular signatures were recorded by the VIMS instrument above different lakes and mares (Kraken, Jingpo, Punga). By modeling the shape of these unique signals and their spread on the surface, it was possible to derive the refractive index of the lakes [3], the methane-ethane ratio [1], the transmission spectrum of Titan's north polar atmosphere [4] and even the roughness of the lake and the height of waves [5-6].

Up to now, the detections of the specular points in the VIMS dataset were conducted manually on the cubes recorded above the North Pole containing a significantly high signal at 5 µm. The purpose of this study is to generalize this detection and create a global database of all the pixels close to the specular points across the entire mission (2004-2017). This will allow us to map the spatial distribution of these points and identify the variability of their spectral signature.

Methodology

Based on Snell-Descartes optical laws, the reflection of a point light source on a perfect flat mirror is located on the mid-plane between the source and the observer for which the incidence angle is equal to the emergence angle. This point is known as *specular point*. More generally, any surface will produce a peak of intensity (*I/F*) when the incidence and emergence angles are equal and aligned. If the surface is smooth enough, the *I/F* peak can be larger than 1 and it highly depends on the surface properties where the reflection occurs.

In the case of an orbiter observing the surface of a planet, the location of the specular point is not trivial but is solution to the antique "Alhazen's problem" of light reflection on a spherical mirror. The specular angle (when it exists) is one of the roots of a quartic polynomial (Fig. 1).

For each Titan flyby, we extract from the SPICE Kernels the location of Cassini (*SC*) and the position of the Sun (*SS*) in Titan's frame before and after close-approach. Then, we check the presence of the specular point and we calculate its expected location as function of time (Fig. 2). Finally, we compare the VIMS cube pixel coordinates with the specular point to keep only the pixels within 1° around the specular angle.

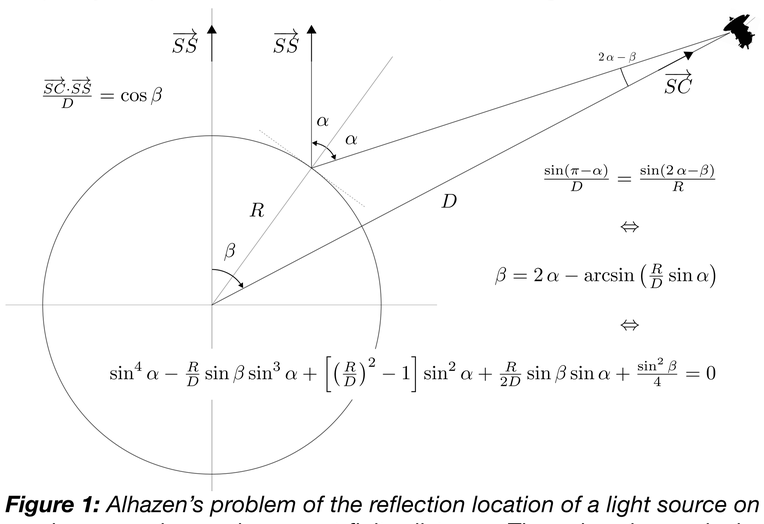


Figure 1: *Alhazen's problem of the reflection location of a light source on a sphere seen by an observer at finite distance. The only unknown is the specular angle alpha.*

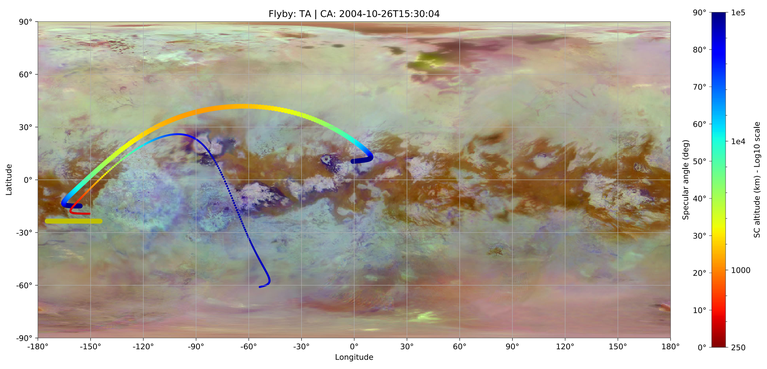


Figure 2: *Locations of the sub-solar point (yellow line), sub-spacecraft point (thick colored line) and specular point (thin colored dots) during TA flyby (Oct 2004) ±16h around closest approach. Background: Titan VIMS-ISS mosaic [7].*

National Aeronautics and Space Administration

Jet Propulsion Laboratory
California Institute of Technology
Pasadena, California

www.nasa.gov

Copyright 2019. All rights reserved.

Results

Between 2004 and 2017, 127 targeted flybys were recorded above Titan. Figure 3 represents the location of the specular point at ±3h around closest approach. We can see that Titan's surface is unevenly covered but most of the main geological units are cross at least once. Due to orbital constrains, the sub-solar point on Titan never gets higher than 26°N, therefore, the smallest specular angle observed on the northern lakes is equal to 45° minimum and is usually between 60° and 80°. This list of tracks is very important to pre-select the spectral-cubes for which the footprint on Titan's surface contains a specular point.

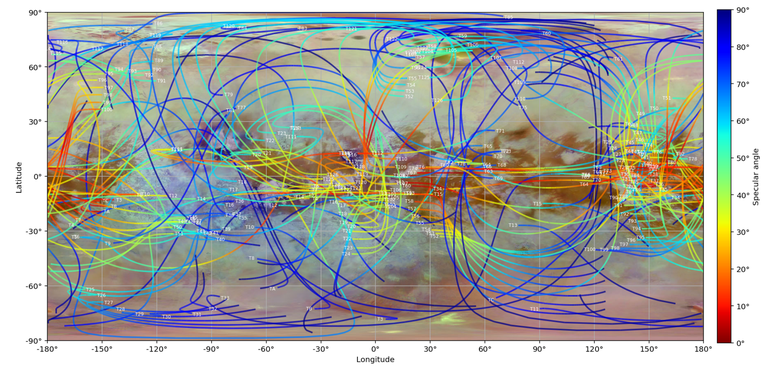


Figure 3: *Locations of all the specular points tracks for the 127 Titan flybys (TA to T126) accounted during the Cassini mission between 2004 and 2017. Each track correspond to ±3h around closest approach.*

Figure 4a provides an example during T104 (2014) when the specular point crossed a VIMS cube footprint (cube *#1787310294_1*). We can check that at the image mid-time, the sub-solar point (*SS*), the specular point and the sub-spacecraft point (*SC*) are aligned on a great circle. The specular point is at equal angular distance between the two other points and the local incidence and emergence angles are equal to the specular angle (51°). In this case, we found 4 pixels matching our 1° criteria (Fig. 4b). They are located on a channel connecting the upper and the lower part of Kraken mare. Their individual spectra are very specific to a specular spectrum on a lake (Fig. 4c). They share the shame global shape, but they present a very strong peak at 5 µm which vary rapidly when the angular distance to the specular point increase. Five additional peaks of intensity can be noticed at 1.58 µm, 2.03 µm, 2.70 µm, 2.79 µm and 2.90 µm.

During the 13 years of mission, Cassini recorded 26,369 resolved cubes on Titan. With our method, we found 2,297 cubes containing at least one specular point in the field of view and 918 cubes contain more than one pixel with a specular geometry. This represent a collection of 7,594 spectra that we stored in a database. Only 141 of them have a *I/F* peak larger than 0.5 in the 5 µm range.

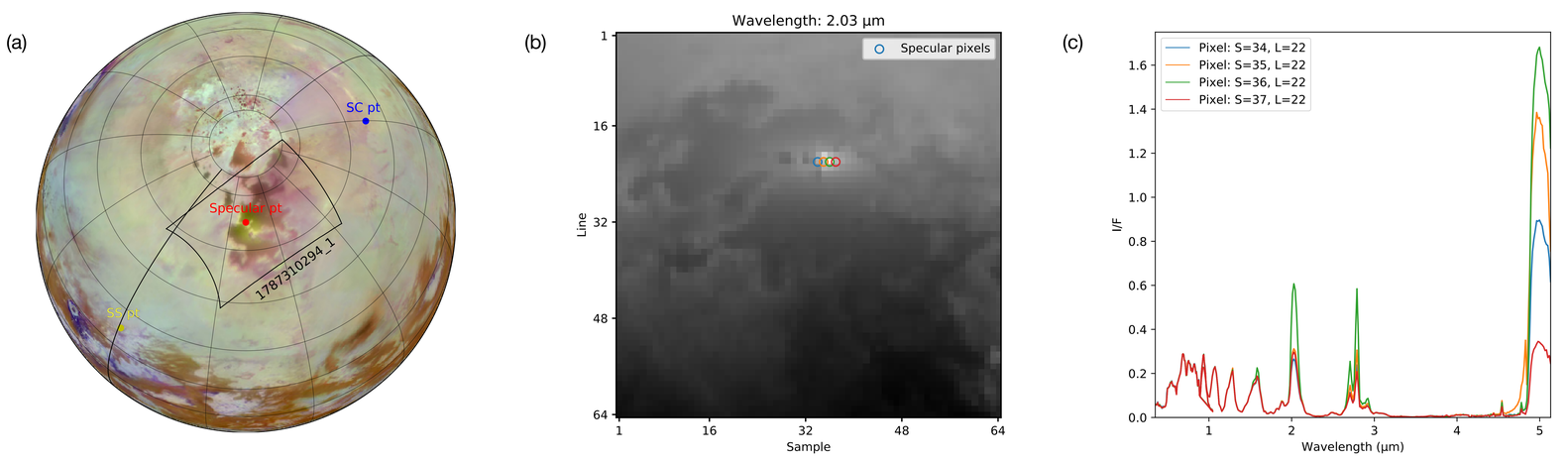


Figure 4: *Example of a specular reflection on cube #1787310294_1 recorded during T104 flyby (Aug. 2014). (a) Specular geometry and cube footprint. The specular angle is equal to 51° (b) VIMS image band at 2.03 µm. The 4 circles correspond to the closest pixels to the specular reflection. (c) Spectra of the 4 selected pixels where a I/F peak can be seen at 1.58 µm, 2.03 µm, 2.70 µm, 2.79 µm, 2.90 µm and 5 µm.*

Figure 5 summarizes the location of all the specular pixels observed around the northern latitudes with a peak intensity higher than 0.5. The size of the circle is proportional to the intensity of the strongest peak and the color represents its wavelength. Most of the pixels with a strong peak at 5 µm are located on Kraken mare (between 30°E, 55°N and 90°E, 80°N), on Kivu lacus (125°W, 87°N) and south of Jingpo lacus (25°E, 72°N). We were able to find all the specular pixels analyzed by previous studies [1, 3-6]. In our case, we keep all the specular pixel independently of their special signature. This allows us to notice that many specular pixels which do not present a strong peak at 5 µm are located on the shores of known lakes. This confirms that the presence of a 5 µm specular peak is highly correlated with the presence of liquid lakes. Finally, in some cases, the signal appears much stronger in the visible channel of VIMS (< 1 µm). For now, these signals are not well understood and could be related to the relative calibration between VIMS-VIS and VIMS-IR instruments.

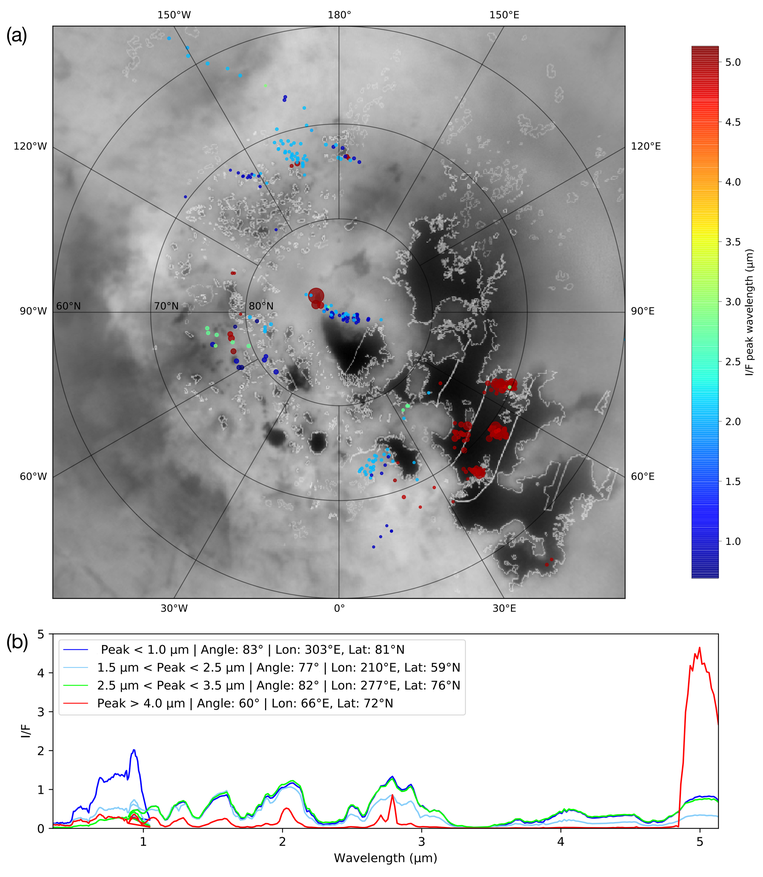


Figure 5: *(a) Locations of all the possible specular pixels on the North Pole recorded between 2004 and 2017. The radar contour of the lakes are reported in white. (b) Examples of specular spectrum observed in this region. Background: ISS mosaic 2018 (PIA22770).*

Discussion and conclusion

This new dataset provides a unique and complete collection of all the cubes of interest containing at least one pixel in a specular geometry. The spectra of these pixels will need to be analyzed with radiative transfer models to determine precisely the properties of the surface on the different reflection area. In some cases, like on Kraken mare, the number of detections is high enough to make statistical analysis of the temporal variability of the surface.

Moreover, by comparing the peak intensity with the direct surrounding pixels, we should be able to provide information on the transmission of the atmosphere and the amount of haze on the line of sight.

Finally, as previous studies already reported [6], bright off-specular pixels play a key role in the detection of wet surfaces and are required to estimate the wave amplitude of the surrounding lakes. The extraction of these pixels is currently not implemented but could be achieve with our current tools.

Tracking specular reflection on the surface of Titan provides many opportunities to probe its surface hidden by its thick hazy atmosphere. We show that the VIMS dataset contains almost 10% of cubes with at least 1 pixel in a specular geometry. This represent a large collection of spectra that could help us to better determine the surface and atmosphere properties, the lake content and behavior and bring new insights on the morphology and composition of the surrounding geological units.

References:

[1] Stephan et al. 2010 - GRL
[2] Stofan et al. 2007 - Nature
[3] Soderblom et al. 2013 - Icarus
[4] Barnes et al. 2013 - APJ
[5] Barnes et al. 2011 - Icarus
[6] Barnes et al. 2014 - Plan. Sc.
[7] Seignovert et al. 2019 - LPSC

Acknowledgments:

B. S. thanks Mike Malaska (3227) for sharing with us its Titan lakes shapefile dataset used in the figure 5.

Poster No. P-02

CL#19-3231

National Aeronautics and Space Administration

Thermal Tides in the Atmosphere of Mars

Liam Steele (3222), Armin Kleinböhl (3222), David Kass (3222) & Richard Zurek (6000)

Jet Propulsion Laboratory, California Institute of Technology. Email: liam.j.steele@jpl.nasa.gov

1. What are thermal tides?

- Global-scale oscillations of temperature, pressure and wind in the atmosphere, forced by (i) the absorption of radiation by aerosols, and (ii) heat transfer from the surface.
- Play a much more significant role on Mars than on Earth.
- Need to gain a better understanding of thermal tides as they can:
  - Influence surface pressure and wind, potentially impacting the initiation of dust storms.
  - Affect the transport and phase of aerosols.
  - Propagate into the upper atmosphere where they can impact spacecraft aerobraking maneuvers, as well as entry, descent and landing (EDL) operations.

2. How do we detect them?

- Use temperature profiles from the Mars Climate Sounder (MCS) instrument in different Mars years (MY). Fig. 1 shows an example of the local time coverage of the data vs latitude.

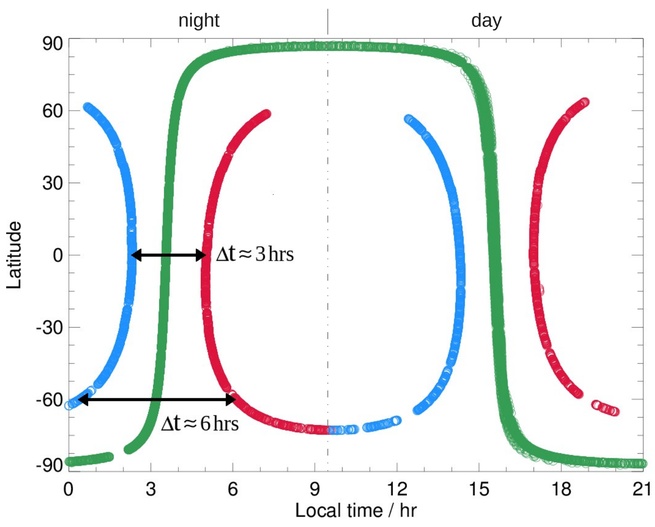


Fig. 1: Variation with latitude of local time coverage of intrack (green), and crosstrack (blue and red) observations from the MCS instrument. We can compare the evolution of tides at three different periods over a time interval of ~3 hrs at the equator and ~6 hrs at ±60º latitude.

- We combine data 12 hrs apart in local time (day and night) to make average temperature fields: $T_{ave} = (T_{day}+T_{night})/2$. Fig. 2 shows an example of T_{ave} in two different Mars years.
- We perform Fourier analysis on T_{ave} to extract amplitude and phase information about the thermal tides at different times.
- Previous studies have used the intrack (green in Fig. 1) data only for Fourier analysis. We also use the crosstrack data (blue and red in Fig. 1). This enables us to investigate the diurnal, as well as seasonal, behaviour of thermal tides, and we can look at times of day not previously analyzed.

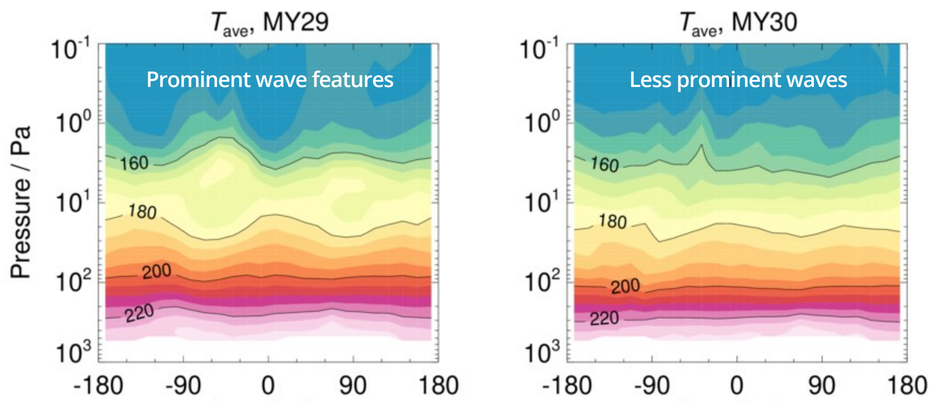
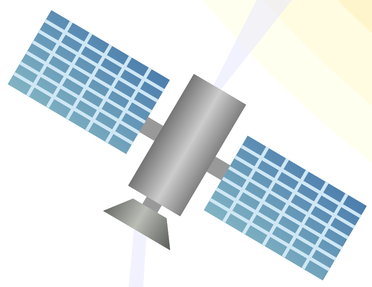


Fig. 2: T_{ave} field (K) between ±15° latitude for southern hemisphere spring equinox in Mars years 29 and 30, using intrack data. MY29 shows strong wave features related to tides.

Conclusions

- **Previously-unseen** large-amplitude tidal features in Mars' tropics have been revealed by performing Fourier analysis on Mars Climate Sounder temperature data.
  - The tides appear linked to **temporal variations** in the nighttime dust (and possibly water ice) distributions.
    - Current computer simulations of Mars' atmosphere (needed for aerobraking and EDL planning) **cannot replicate** the observed tidal features.
      - Results give **new insight** into Mars' atmospheric dynamics, and reveal the need for **improved understanding** of the dust and water cycles from spacecraft data and models.



3. What have we discovered?

- Thermal tides seen in MY29 intrack data during southern hemisphere spring equinox (Fig. 2) are not visible in other years.
- Large-amplitude tides do appear when we look at MCS crosstrack data, with nighttime temperatures showing large-amplitude waves (Fig. 3, top), which seem related to the diurnally-varying dust distribution (Fig. 3, bottom).

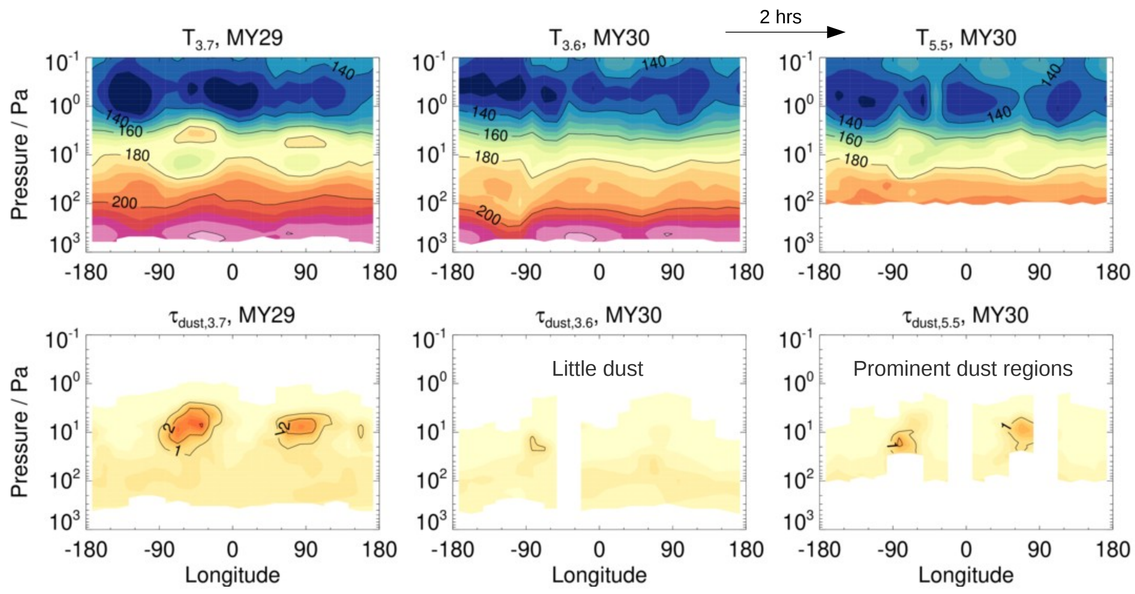


Fig. 3: Temperature (top, K) and density-scaled dust opacity (bottom, 10^{-3} m^2 kg^{-1}) from MCS nighttime data, averaged between ±15° latitude. MY29 panels show intrack data with an average local time of 3.7am. MY30 panels show intrack data (average time 3.6am) and crosstrack data (average time 5.5am).

- To try and understand these results, we performed a similar analysis using data from the Ensemble Mars Atmosphere Reanalysis System (EMARS) computer simulation, the current best representation of Mars' atmosphere.
- The behaviour seen here is not present in the EMARS simulation, which could impact aerobraking and EDL planning which require the use of atmospheric models.
- More work is needed to understand the dynamics responsible for the varying dust distribution, its effect on thermal tides, and why Mars year 29 is different to the other Mars years observed by MCS.

National Aeronautics and Space Administration

Jet Propulsion Laboratory
California Institute of Technology
Pasadena, California

www.nasa.gov

Copyright 2019. All rights reserved.

Poster No. P-03

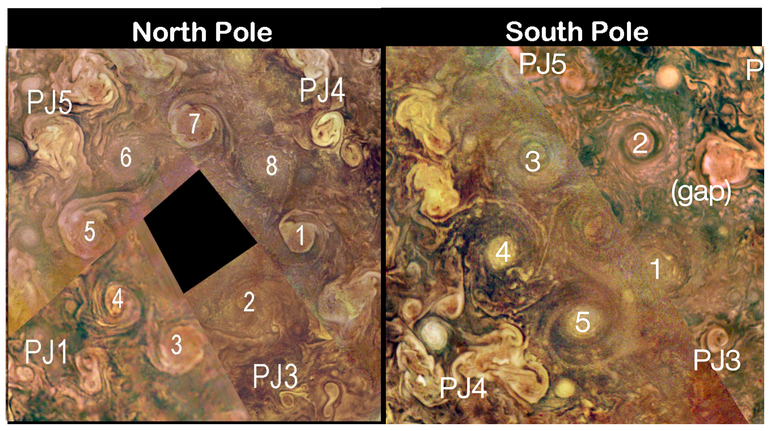
National Aeronautics and Space Administration

Tracking the long-term evolution of the circumpolar cyclones on Jupiter with Juno

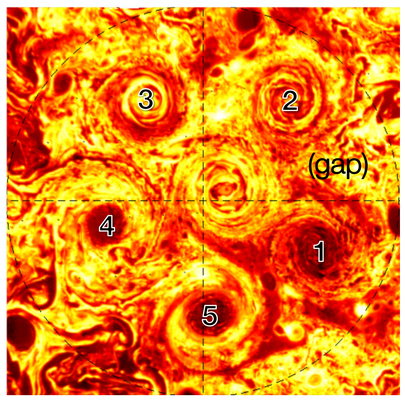
Author: Fachreddin Tabataba-Vakili (3222), Tom Momary (3222), James Sinclair (3222), Glenn Orton (3222)

1 Introduction

Context: NASA's Juno spacecraft is currently observing Jupiter's polar regions with unprecedented spatial resolution (Orton et al. 2017, Adriani et al. 2018). Observations with the JunoCam (Hansen et al. 2017) and JIRAM (Jovian Infrared Auroral Mapper, Adriani et al. 2017) instruments have revealed apparently stable constellations of cyclonic vortices, surrounding both the north and south poles, an unprecedented phenomenon that has never been observed in a planetary atmosphere. While theoretical simulations of the Jovian polar atmosphere have predicted highly turbulent environment (e.g. Cho and Polvani, 1996; O'Neill et al. 2015), no computational atmospheric models have resulted in these stable geometric structures. The south pole is surrounded by five circumpolar cyclones (CPC), the north pole by eight CPCs.



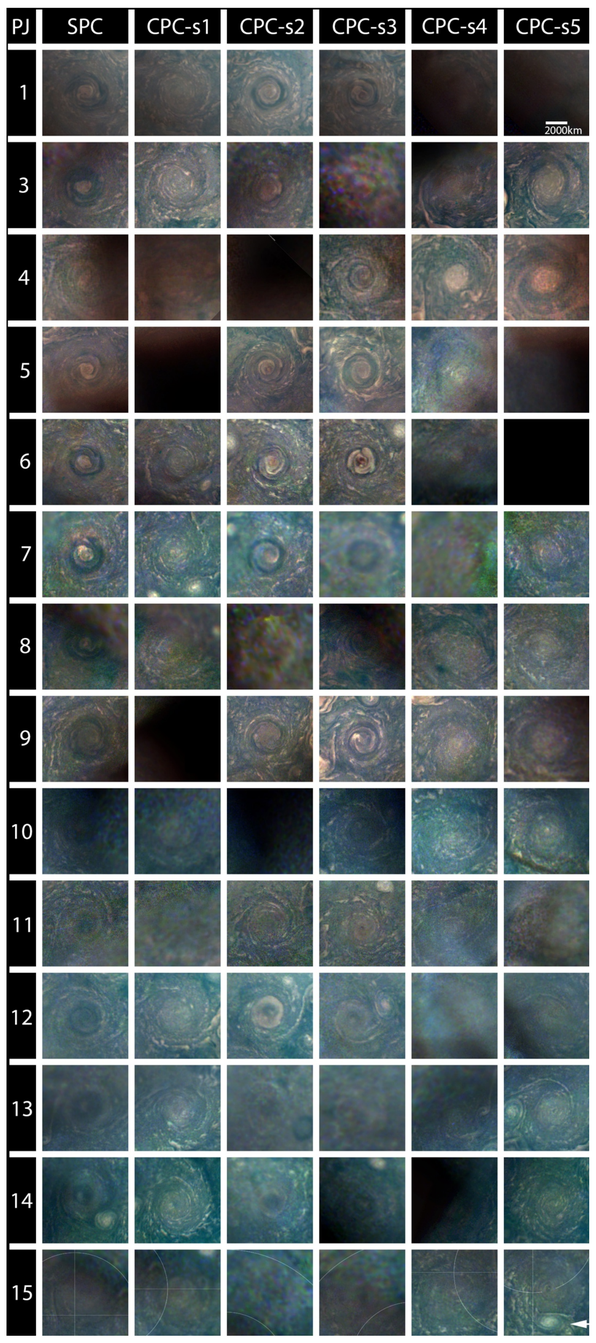
Composite image of circumpolar cyclones observed with JunoCam at the North and South Poles of Jupiter. PJ (perijove) signifies the particular orbit in which Juno was closest to Jupiter when measurements were taken. PJs are separated by 53 days.



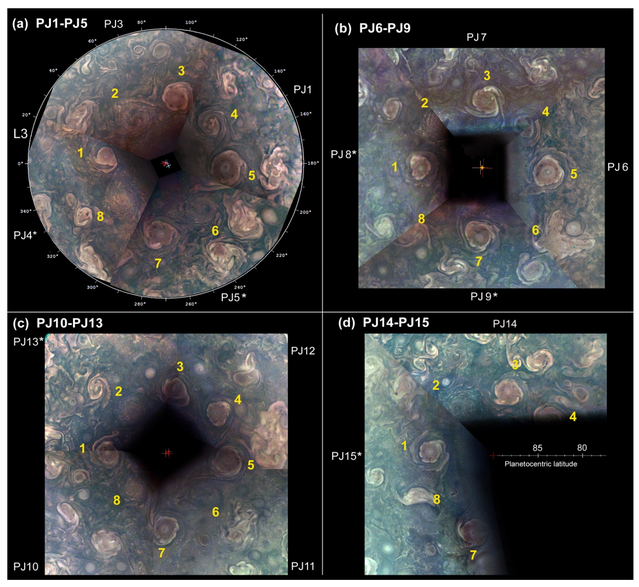
JIRAM observation of the south polar circumpolar cyclones during PJ4. Adapted from Adriani et al. (2018).

Question: How stable are these CPC constellations? How do they evolve in the long-term?
Below we investigate the long-term stability and behavior of the circumpolar cyclones in detail.

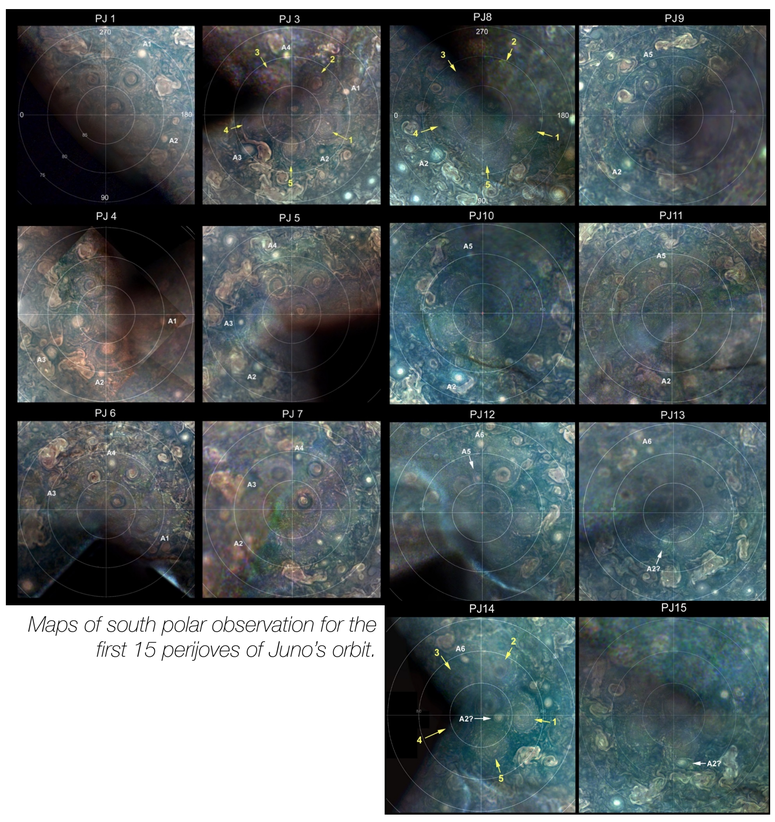
2 Observations



Evolution of the morphology and southern circumpolar cyclones and their immediate vicinity.

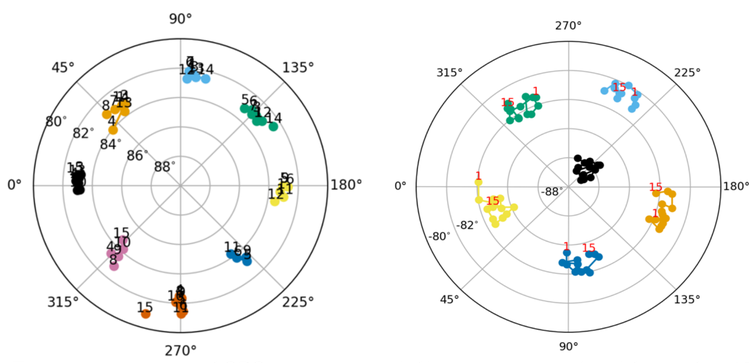


Composite maps of north polar observation, the north pole is in darkness due to north polar winter.

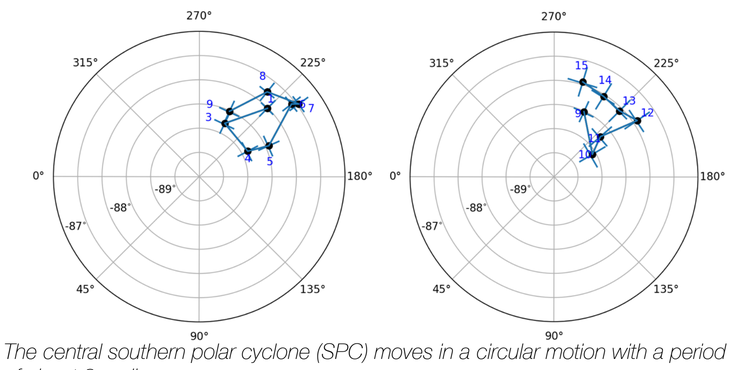


Maps of south polar observation for the first 15 perijoves of Juno's orbit.

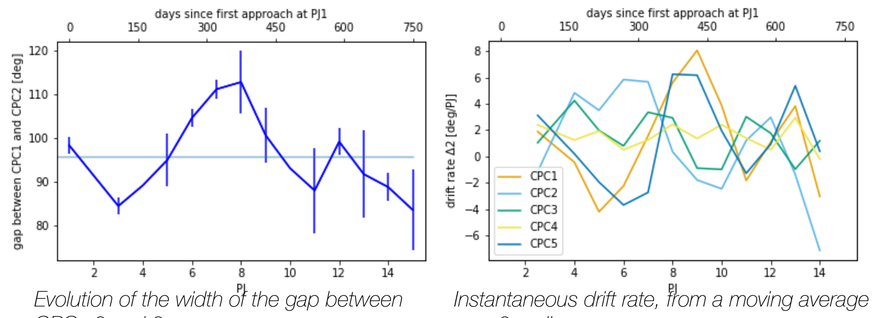
3 Results



Tracking the location of CPCs on the north (left) and south pole (right) for the first 15 perijoves of Juno's orbit. On the south pole there is a systematic westward drift. On the north pole no systematic drift is observed.



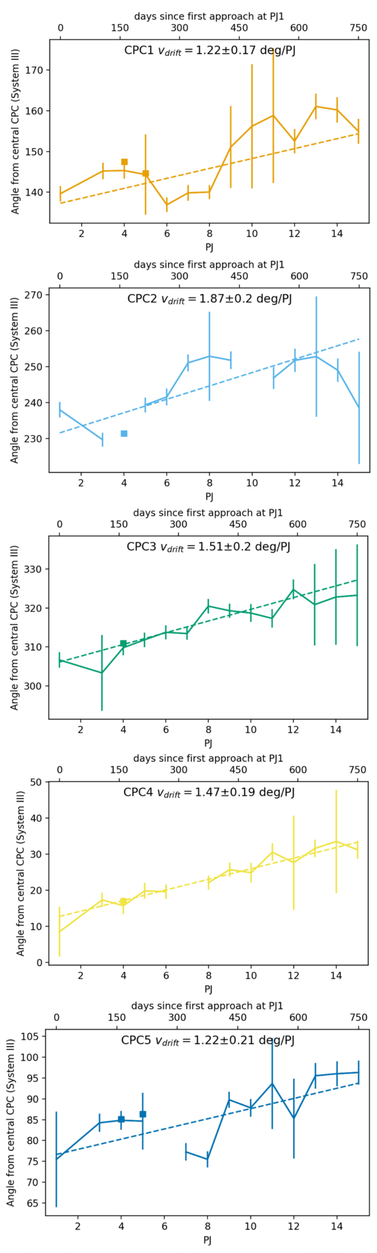
The central southern polar cyclone (SPC) moves in a circular motion with a period of about 8 perijoves.



Evolution of the width of the gap between CPCs 2 and 3.

Instantaneous drift rate, from a moving average over 3 perijoves.

The mean drift rate shows that the pentagonal circumpolar cyclone pattern steadily rotates about its center with an average rotation rate of 1.5 deg/PJ or 0.004 m/s. This background drift is superimposed by the variable behavior of each CPC. The drift rates show that the movement of CPCs 3 and 4 are coupled throughout the whole observation period. From PJ7 onwards CPCs 1 and 2 also show a similar behavior in drift rate. CPCs 2 and 3 have anticorrelating drift rates. This anticorrelation contributes to strong variation of the width of the gap.



Angular position of the southern CPCs with reference to the central south polar cyclone. The filled dots are JIRAM measurements during PJ 4 and 5 (Adriani et al., 2018).

4 Connection to Vortex Crystals

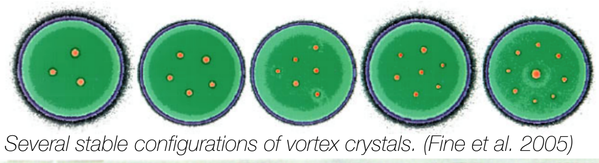
Vortex crystals are characterized by a stable, symmetric configuration of vortices around a circle. So far, real life examples of this phenomenon have only been observed in experiments of rotating superfluid helium and Bose-Einstein Condensates, as well as electron columns and super-conductors placed in magnetic fields.

In theory vortex crystals can emerge in an inviscid two-dimensional fluid due to the relaxation of a turbulent initial state into a state of maximum entropy (Jin and Dubin 1998). In reality, however, without further energy input even the constellations of vortex crystals decay with time due to minute viscous forces (Fine et al. 1995).

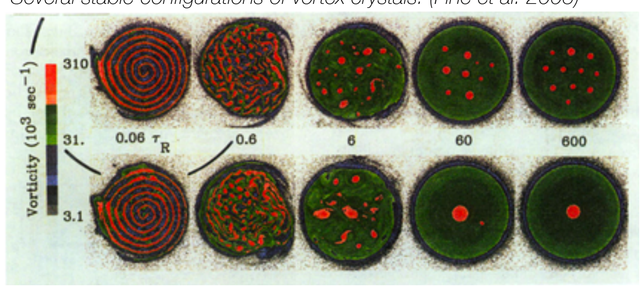
Overall, shape and long-term behavior of the CPCs match well with vortex crystal theory. This is surprising, considering that Jupiter's atmosphere is much more complicated than a 2d fluid. An internal heat source, more lightning detections near the poles, points towards deep convection.

Open Questions:

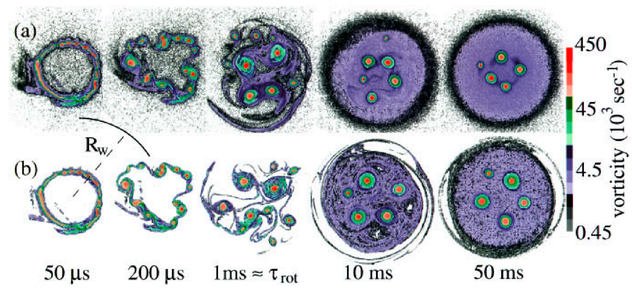
- Is the 2d vortex crystal mechanism respon-sible for the CPCs by dominating over 3d effects? Or is a different mechanism at play?
- Where does the turbulent energy come from to keep them from decaying?
- The beta effect is pushing cyclones towards the poles. Why don't they merge at the pole?



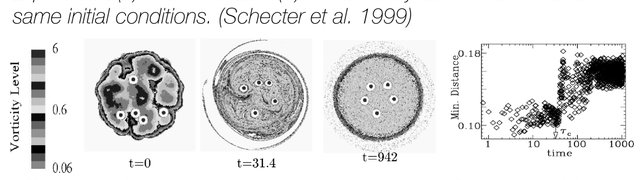
Several stable configurations of vortex crystals. (Fine et al. 2005)



The evolution of two vortex experiments with slightly different viscosities. (Fine et al. 2005)



Experiment (a) and simulation (b) of vortex crystal evolution with the same initial conditions. (Schecter et al. 1999)



Evolution of a simulated vortex crystal over time. Reproduced from Jin & Dubin (2000). Snapshots depict the initialization (t=0), 'vortex cooling' (t=31.4), and equilibrium (t=942) phases of vortex crystal evolution. The plot on the right depicts the variability of the minimal distance between any two vortices in the quasi-stable vortex crystal state.

Poster No. P-04

National Aeronautics and Space Administration

Jet Propulsion Laboratory
California Institute of Technology
Pasadena, California

www.nasa.gov

Copyright 2019. All rights reserved.

References:

Adriani A., et al. "Clusters of cyclones encircling Jupiter's poles." Nature (2018).
Adriani, A., et al. "JIRAM, the Jovian infrared auroral mapper." Space Science Reviews 213.1-4 (2017): 393-446.
Cho, J.Y-K., and L.M. Polvani. "The emergence of jets and vortices in freely evolving, shallow-water turbulence on a sphere." Physics of Fluids 8.6 (1996).
Fine, K.S., et al. "Relaxation of 2D turbulence to vortex crystals." Physical review letters 75.18 (1995)..
Hansen, C.J., et al. "Junocam: Juno's outreach camera." Space Science Reviews (2014).
Jin, D.Z., and D.H.E. Dubin. "Regional maximum entropy theory of vortex crystal formation." Physical review letters 80.20 (1998).
O'Neill, M.E., K.A. Emanuel, and G.R. Flierl. "Polar vortex formation in giant-planet atmospheres due to moist convection." Nature Geoscience 8.7 (2015).
Orton, G.S., et al. "The first close-up images of Jupiter's polar regions: Results from the Juno mission JunoCam instrument." Geophysical Research Letters (2017).
Schecter, D. A., et al. "Vortex crystals from 2D Euler flow: Experiment and simulation." Physics of Fluids (1999).

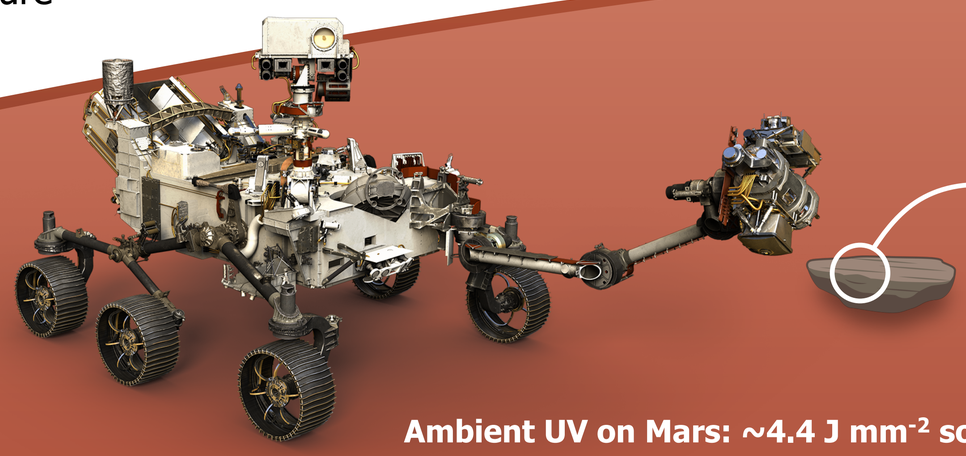
National Aeronautics and Space Administration

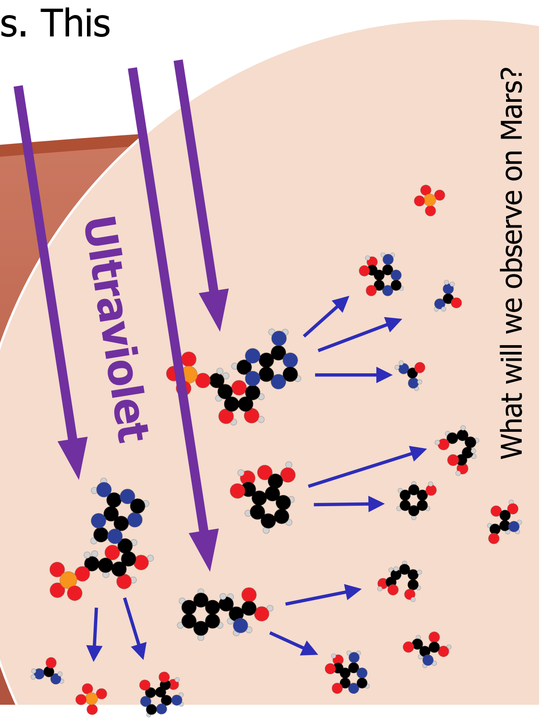
In Situ Alteration of Organic Biosignatures in Perchlorate-Spiked Martian Regolith Analog

Joseph Razzell Hollis (3225), Teresa Fornaro (Carnegie), William Rapin (6300 Caltech), Jessica Wade (Imperial College London), Andrew Steele (Carnegie), Rohit Bhartia (3225), Luther Beegle (3200)

Mars' lack of atmosphere means little protection from UV light, which can photochemically alter organic compounds. This means the sub-surface may be the best place to find intact chemical biosignatures.

Deep-UV Raman spectroscopy can provide insight into the alteration of these compounds over time, through *in situ* exposure to our 248.6 nm laser





Ambient UV on Mars: ~4.4 J mm^{-2} sol^{-1}
Typical SHERLOC measurement: ~0.8 J mm^{-2} @ 248 nm

[1] Fornaro et al. (2018). *Life* 8, 56. doi: 10.3390/life8040056.
[2] Scappini et al. (2004). *Int. J. Astrobiol.,* 3, 17–19. doi: 10.1017/S147355040400179X
[3] González et al. (2010). *J. Geophys. Res.* 115, 1–11. doi:10.1029/2010JE003599.

Clays as Organic Preservers

Minerals can catalyze reactions and suppress them. This has profound implications for the preservation of organic biosignatures in Martian regolith/mudstones.[1]

Certain clays, such as montmorillonite, are known to adsorb biomolecules such as DNA and protect them from UV-induced degradation.[2]

The presence of ClO_4^- (Perchlorate) ions in Martian regolith may also accelerate chemical degradation.[3]

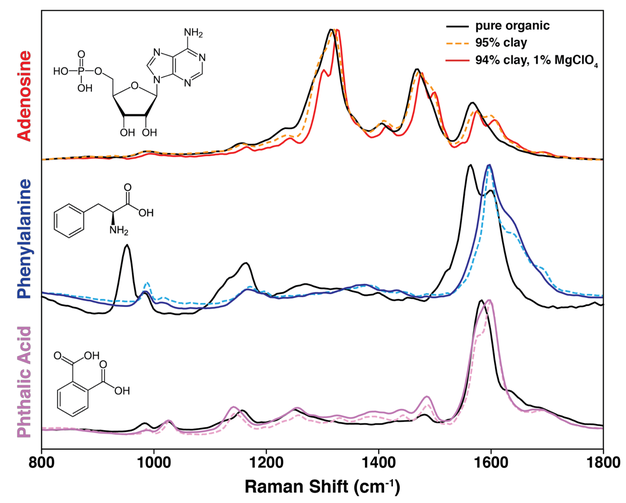
Deep-UV Raman spectroscopy

Raman peaks tell us about **molecular vibrations**, and are highly sensitive to changes in chemical structure.

Deep-UV resonance selectively **enhances** Raman from vibrations of the **aromatic ring**

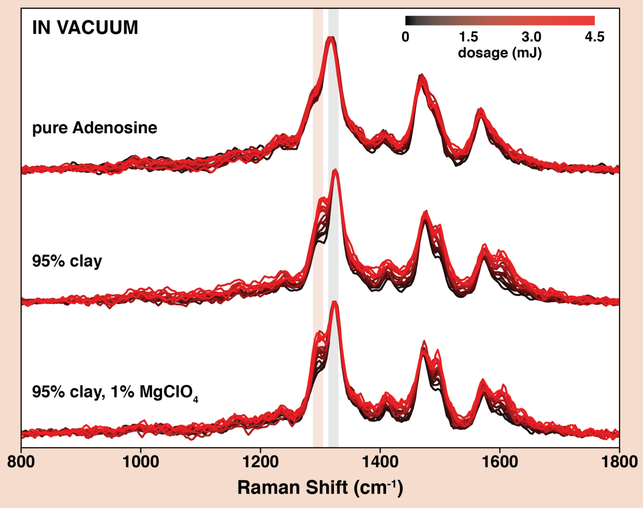
All 3 molecules show altered spectra when mixed with clay and/or perchlorate and measured.

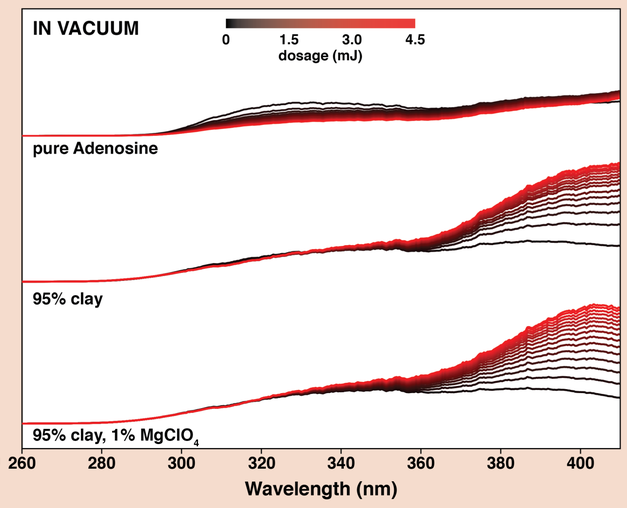
Visible discoloration of exposed area suggests degradation



In Situ Exposure of Adenosine Phosphate

Repeated **short** exposures (~100 pulse, ~0.3 mJ) in **vacuum** reveal how spectra change with UV dosage





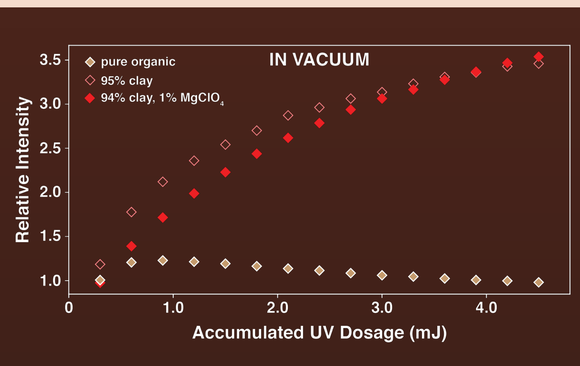
Spectral changes are identical in **air**, but occur faster and go further

Photo-oxidation?

Pure Adenosine:
- No change in Raman, loss of fluorescence
- Suggests direct breaking of aromatic ring

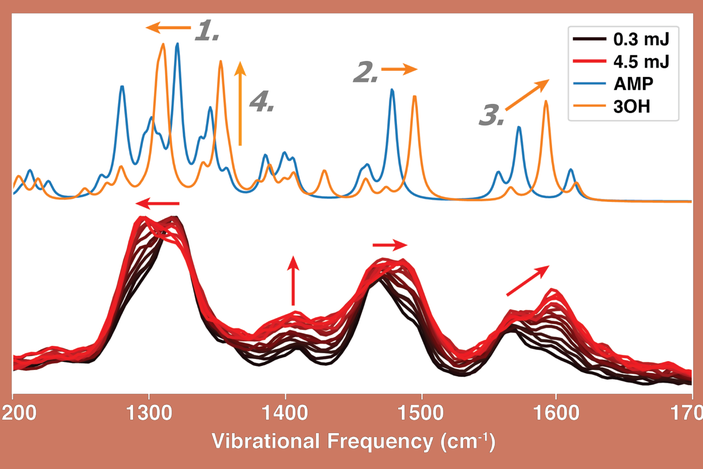
In Clay:
- New Raman peaks develop with dosage
- Fluorescence increases at **>360 nm**
- Formation of altered aromatic ring?

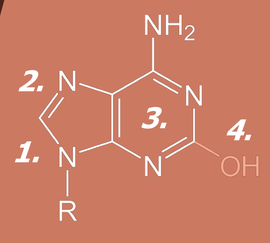
With Perchlorate:
- Similar to clay, change occurs faster



DFT Simulations

Several intermediate oxidation products were modelled to see if any can produce the observed spectral changes for degraded adenosine in the presence of clay.

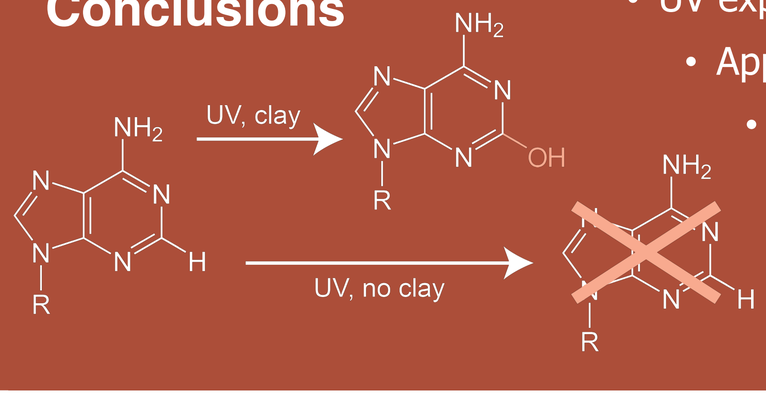




Addition of electron withdrawing group next to π-system causes bonds to vibrate at different frequencies (***1.-3.***), creates new vibration (***4.***)

Raman changes consistent with a **hydroxylated** adenine ring

Conclusions



- UV exposure can **alter** organic compounds, even under **vacuum**
  - Appears to be a **photo-oxidation**, reduces fluorescence
    - Presence of clay limits reaction to **hydroxylation**
      - Impact of **Perchlorate** is relatively minor
        - Oxidizer may be **O_2/H_2O** trapped in mineral matrix

National Aeronautics and Space Administration
Jet Propulsion Laboratory
California Institute of Technology
Pasadena, California

www.nasa.gov

Copyright 2019. All rights reserved.

Poster No. P-06

National Aeronautics and Space Administration

Seismic structure of icy moons from full waveform modeling

Saikiran Tharimena (3226)
Mark Panning (3226), Steven Vance (3226)

Motivation: Our understanding of Earth's internal structure and composition evolved with the advancement of seismology. Extending seismic investigations to planetary bodies, primarily the icy moons of Jupiter and Saturn, has far-reaching implications for our understanding of their internal structure, composition and thus the habitability of planetary interiors. Icy moons are almost certainly seismically active with energy sources in the form of tidal cracking, turbulence in the subsurface ocean, and/or bolide impact. Given the possibility of future missions to deploy seismometers on these moons, it is essential to consider design of possible seismic experiments and quantify plausible seismic activity.

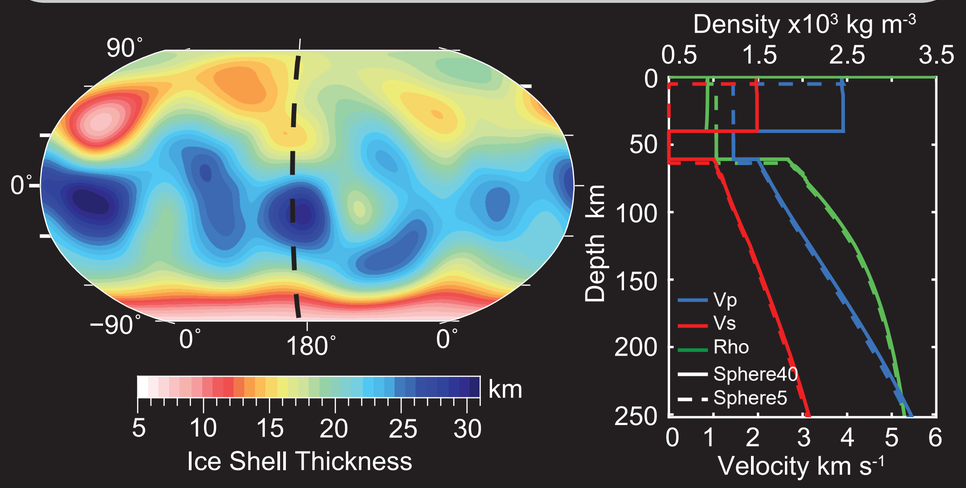


Figure 1:
(a) Global ice thickness model of Enceladus [1]. Inset shows the ROI for high-res 3D simulation
(b) Interior structure (Vp, Vs, Rho) model [2] used in the global and regional meshes

Full waveform modeling: We model the full 3D seismic wavefield on Enceladus (Fig 2) using state-of-the-art spectral element solver called Salvus [3]. We designed high-resolution 3D meshes at both global (5s) and regional (2s) scales, incorporating variations in ice shell thickness. We generated synthetic seismograms for 4 scenarios; spherically symmetric global model with 5km and 40km thick ice shell, global model with varying ice shell thickness (Fig1a), and regional model with varying ice shell thickness. We simulate a double couple source of magnitude 3.7 Mw located at 85º S 170ºE, and at a depth of 3 km inside the ice shell.

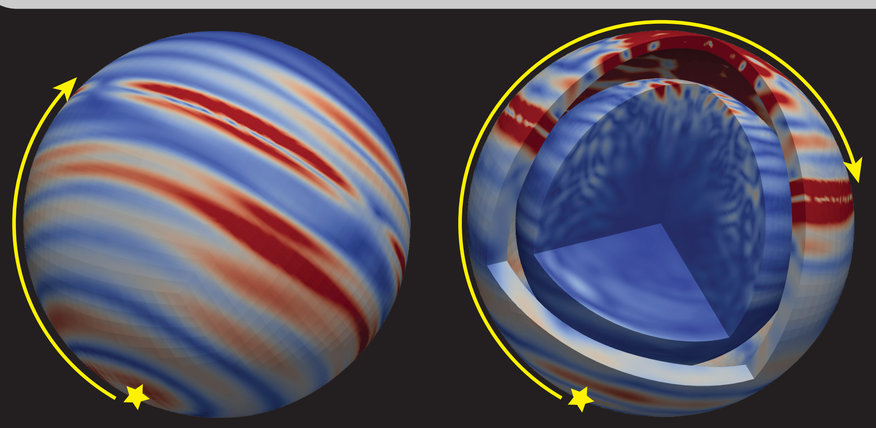
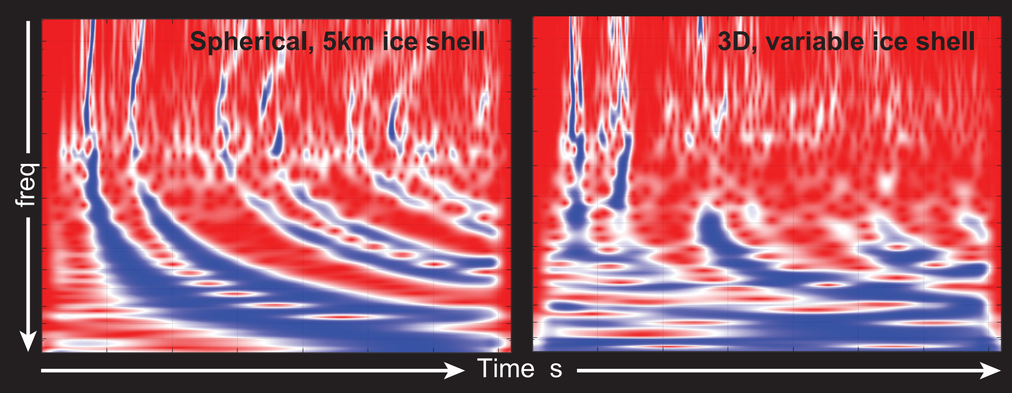


Figure 2: Visualization of seismic wavefield propagating through a global model at (a) 260s and (b) 670s after the "icy moon-quake".



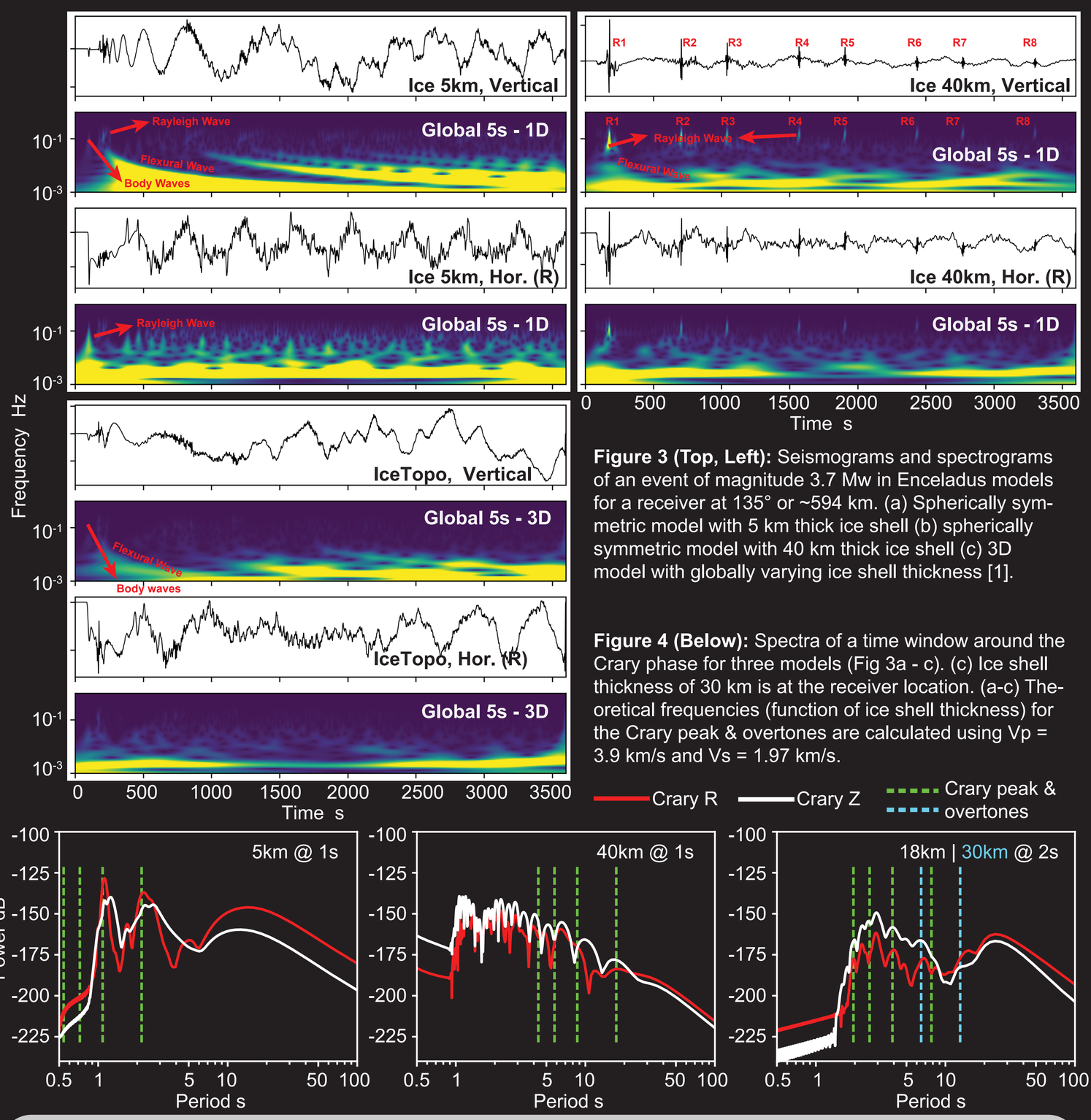


Figure 3 (Top, Left): Seismograms and spectrograms of an event of magnitude 3.7 Mw in Enceladus models for a receiver at 135° or ~594 km. (a) Spherically symmetric model with 5 km thick ice shell (b) spherically symmetric model with 40 km thick ice shell (c) 3D model with globally varying ice shell thickness [1].

Figure 4 (Below): Spectra of a time window around the Crary phase for three models (Fig 3a - c). (c) Ice shell thickness of 30 km is at the receiver location. (a-c) Theoretical frequencies (function of ice shell thickness) for the Crary peak & overtones are calculated using Vp = 3.9 km/s and Vs = 1.97 km/s.

Crary R Crary Z Crary peak & overtones

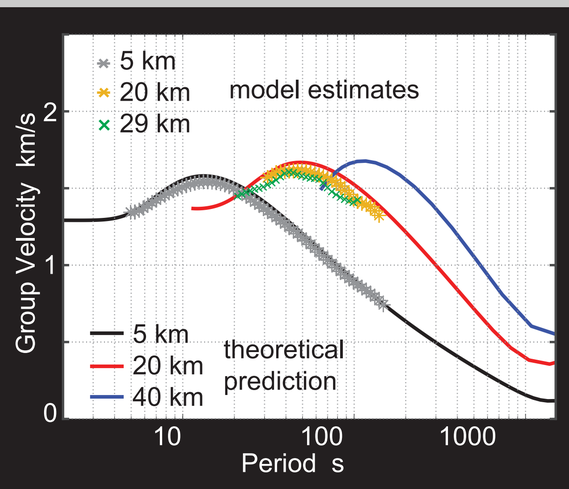
Estimating Ice Shell Thickness:
The two most prominent phases, flexural wave and Crary phase can be used to determine the ice shell thickness, which is probably the most important scientific objective of any mission to the icy worlds.

1) Flexural waves are long period vertically polarized surface waves that travel as full-layer waves. It has an intrinsic dispersion ($c_{fl} \propto \sqrt{f}$) that is independent of the velocity gradient in the ice. As a result, the short periods arrive first and group velocity of long periods goes to zero. The cutoff frequency is where the flexural wave transitions to the Rayleigh wave regime. Rayleigh waves are short period surface waves that have little to no dispersion due to the very small velocity gradient in ice.
2) Crary waves are monochromatic waves that arise due to *SV* waves being completed reflected at critical angle for *SV-P* conversion on the boundaries of ice. The harmonic spectrum of the phase, is characterised by f_{cr}. Measurement of f_{cr} constrains the ice thickness, if V_S and V_P are known.

$$f_{cr} = \frac{(n+1)V_s}{2d\sqrt{1-(V_s/V_p)^2}}$$

Figure 5 (left): Dispersion envelopes for a seismogram recorded at a distance of 120°. Average ice shell thickness along path of wave propagation is 29 km for the varying ice shell model.

Figure 6 (right): Theoretical dispersion curves compared to the estimates from models.



Future Work:
1) Use body waves, including converted an reflected phases, to infer deep interior structure
2) Test robustness of inversion techniques to 3D structure
3) Test detectability of active sources ("Stuff Spewing Edifices") in the south polar region of Enceladus
4) Extend study to include realistic background seismic noise along with likely magnitudes and frequency of event occurance

National Aeronautics and Space Administration
Jet Propulsion Laboratory
California Institute of Technology
Pasadena, California
www.nasa.gov

Copyright 2019. All rights reserved.

References: [1] Cadek et al. Long-term stability of Enceladus' uneven ice shell. *Icarus (2018).* [2] Vance et al. Geophysical investigations of habitability in ice-covered ocean worlds. *J.Geophysical Research Planets (2018).* [3] Afanasiev et al. Modular and flexible spectral-element waveform modeling in two and three dimensions. *Geophysical Journal International (2019).*

The authors acknowledge the support of the developers at Mondaic AG (mondaic.com) for providing the Salvus [3] software package for this research.

P - 07

National Aeronautics and Space Administration

Retiring risks for sample handling and biomarker analysis for Ocean Worlds

Victor Abrahamsson (3227)

Bryana Henderson (3227), **Fang Zhong** (382), **Isik Kanik** (3220) **and Ying Lin** (4210)

Overview

In-situ biomarker detection instrument and methodology have been developed

Existing risks are reduced by completely avoiding organic solvents, organic additives and derivatization reagents

Polar (e.g., amino acids) and nonpolar (e.g., free fatty acids) are analyzed by using water and CO_2, respectively

Risks in life-detection instruments

Contamination: Wet-chemistry laboratory suites on Phoenix and Curiosity Mars landers leaked and confounded results

Degradation: High-temperature techniques (pyrolysis) used on the Vikings, Phoenix and Curiosity mostly yielded debatable data due to degradation and chemical reactions with **salts**

Derivatization & reaction chemistry often burdens current in-situ instrumentation and masks detection and identification of unknown organic compounds

Our solution

Avoid contamination, degradation, and derivatization by using only non-organic solvents to detect and identify biomarkers:

- Supercritical CO_2 – nonpolar (free fatty acids, polycyclic aromatic hydrocarbons and polycyclic aromatic compounds)
- Water – ionic polar (including chiral amino acids) *(On-going development)*
- Superheated water – neutral polar (nucleobases) *(On-going development)*

Chemical analysis in four steps:

1. Extraction **2. Preconcentration**

3. Separation **4. Detection**

National Aeronautics and Space Administration
Jet Propulsion Laboratory
California Institute of Technology
Pasadena, California

www.nasa.gov

Copyright 2019. All rights reserved.

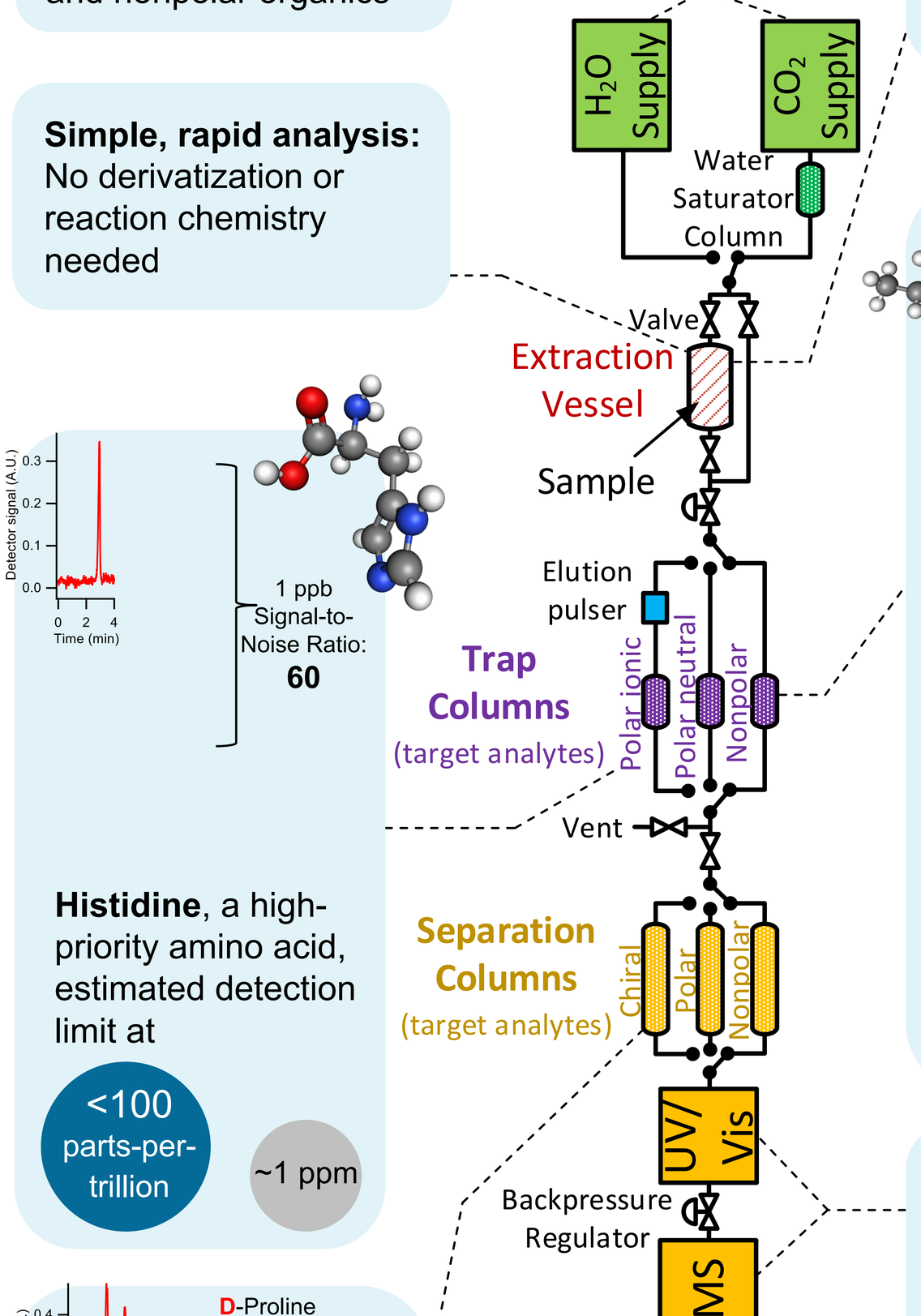
Funded by NASA's Concepts for Ocean Life Detection Technology (COLDTech) Program

Highlighted features and results

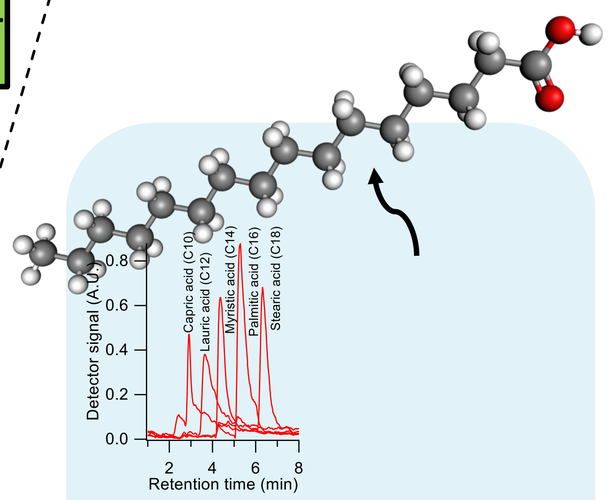
Non-reactive: CO_2 and water solvents enable analysis of both polar and nonpolar organics

Simple, rapid analysis: No derivatization or reaction chemistry needed

The System



Flexible: Silica support material enables aqueous, solid, suspension and/or ice samples



Analysis of **free fatty acids** at parts-per-billion concentration levels from **brines** with

27.5% salt

<40 ppb LOD

~1 ppm LOD

Histidine, a high-priority amino acid, estimated detection limit at

<100 parts-per-trillion

~1 ppm

Chiral separation of proline (100 parts-per-billion of each isomer)

Parts-per-trillion

~1 ppb

Detection limits at parts-per-trillion have been achieved for polycyclic aromatic hydrocarbons and polycyclic aromatic compounds

Compatible: Supports spectroscopy and mass spectrometry detectors, for identification of unknown organic compounds

Our instrument

Reported for Sample Analysis at Mars (Curiosity)[1]



Poster No. P-08

[1] K. Biemann, Proc. Natl. Acad. Sci. U.S.A. **104** (2007), 10310-10313; J. Eigenbrode et al., Science **360** (2018), 1096-1101; P. Mahaffy et al., Space Sci Rev **170** (2012), 401-478; D. Meunier et al., Adv Space Res **39** (2007), 337-344; F. Stalport et al., Planet Space Sci **67** (2012), 1-13; A. Williams et al., Astrobiol **19** (2019), 522-546

Laboratory studies of methyl halides in interstellar ice analogues

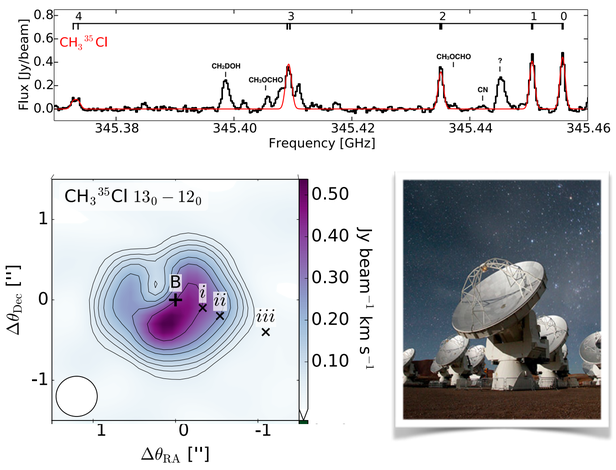
National Aeronautics and Space Administration
Jet Propulsion Laboratory
California Institute of Technology
Pasadena, California
www.nasa.gov

Edith Fayolle (3227), Robert Hodyss (3227), Pierce van Mulbregt (3227), Paul Johnson (322), Aaron Noell (389U)
Jet Propulsion Laboratory, California Institute of Technology

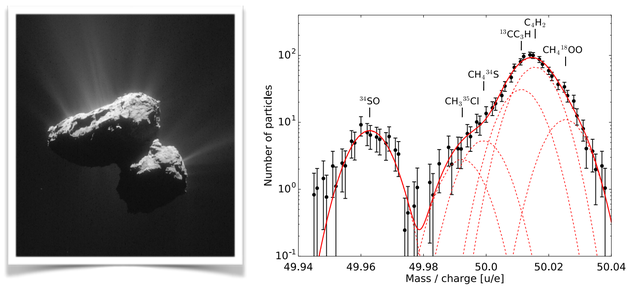
Context and motivation

Methyl halides, CH_3X with X a halogen (F, Cl, Br, I...), are abundant on the Earth where they are mainly produced through industrial and biological processes.

CH_3Cl has recently been observed toward a low-mass protostar, connecting organic and halogen interstellar chemistries.



ALMA spectrum and CH3Cl moment 0 map towards protostar IRAS16293-2422B



NAVCAM and ROSINA-DFMS spectra of 67P/C-G coma

CH_3Cl has also been observed around comet 67P/C-G with an abundance similar to protostars.

Due to their main production source on Earth, methyl halides have been suggested as biomarkers if observed in exoplanetary atmospheres.

Methyl halides can form abiotically before terrestrial planet formation.

Can methyl halides observed in planetary atmospheres, including in our own Solar System, be inherited from pre- and protostellar ices?

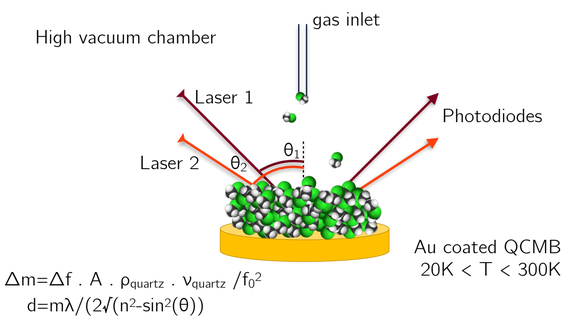
⇒

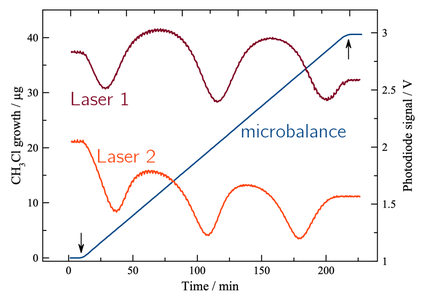
We measured band strengths in pure and H_2O-mixed ices to quantify methyl halides abundance in protostellar ices.

We derived sublimation energies of methyl halides under star- and planet-forming region conditions to assess their ice-gas partitioning.

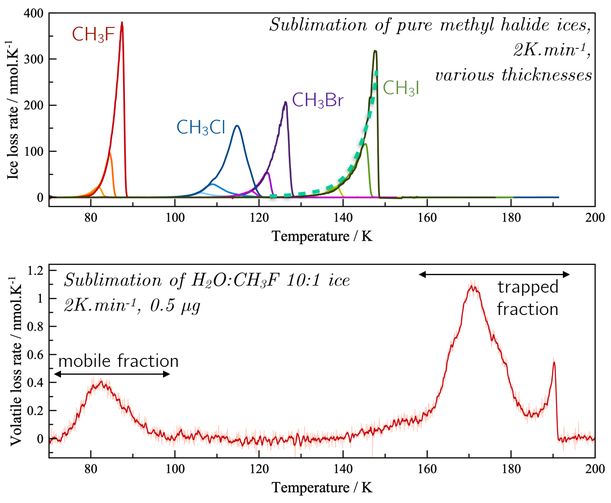
Deposition and sublimation results

- A cryogenically cooled quartz crystal microbalance in high vacuum is used to grow methyl halide ice films, pure and in H_2O mixtures.
- Refractive index, thickness, and thus density are measured by monitoring interference fringes and mass increase during ice growth.





- Ice sublimation is studied by linearly warming the ice film and monitoring the ice loss versus time (temperature).

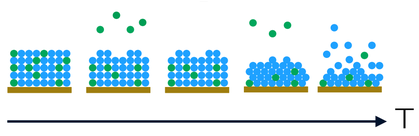


d(ice loss)/dt= ν . exp(-E_{des}/T)



E_{des} : energy to overcome physisorption
ν : attempt frequency

Sublimation of bulk CH_3X is limited by formation of a H_2O-rich ice surface



Methyl halide	Ref. index (633 nm)	Density (20K, g.cm^{-3})	Sublimation energy	Snowline protostars	Trapping 10:1 H_2O:CH_3X
CH_3F	-	-	2470 K	50 K	78%
CH_3Cl	1.12	0.82	3300 K	70 K	>90%
CH_3Br	1.28	1.73	3660 K	77 K	- %
CH_3I	1.52	2.42	4250 K	90 K	- %

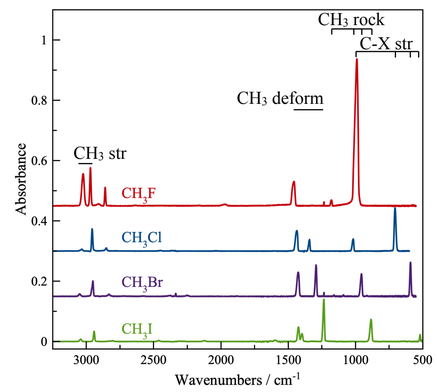
Interpretation and impact

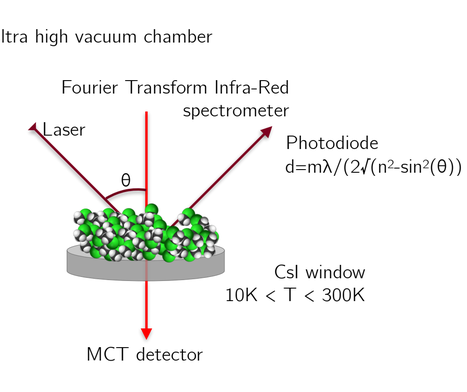
- The C-X and CH_3-rock vibrations of methyl halides are good diagnostics for quantifying CH_3X abundance and probing the ice environment.
- Despite CH_3F abundances predicted to be slightly lower than CH_3Cl in protostars, the strong C-F stretch may compensate for its detection.

- The desorption energy of methyl halides is not strictly controlled by the species molecular mass. Size and polarity matters.
- CH_3Cl sublimates at about T= 70K, ~130 AU for a low-mass protostar, consistent with gas phase detections. CH_3F sublimates further out (~260 AU), making it more difficult to be detected by interferometers.

Spectroscopic results

- Methyl halide ice films, pure and in H_2O mixtures are deposited onto a cryogenically cooled CsI window, their thickness monitored during deposition by laser interferometry, and their mid-IR spectrum interrogated by FTIR

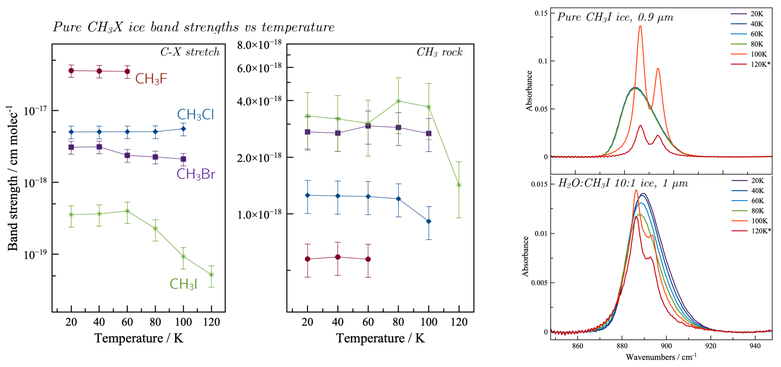




- Band strength for CH_3X vibrational bands are obtained by integrating the band optical depth divided by the ice column density

- Water ice and temperature strongly affects the CH_3X vibrational bands

  They can be used as diagnostics of the ice structure in astrophysical spectra



*Desorption onset

Copyright 2019. All rights reserved.

Poster No. P-09

National Aeronautics and Space Administration

Studying table salt to understand Europa's surface history

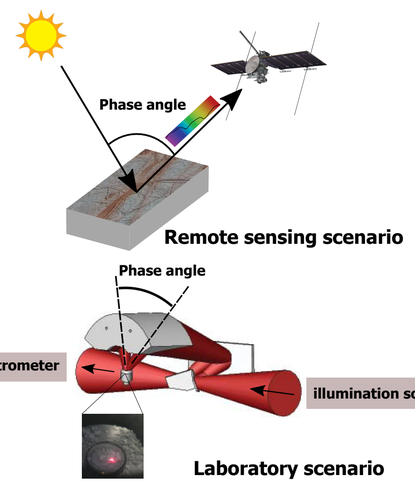
Author: Bernhard Jost (3227)
Paul V. Johnson (322), Robert Hodyss (3227)

Scientific problem in a nutshell

Most salts are spectrally neutral across the visible and infrared wavelength range and are therefore hard to detect by remote sensing.This is especially true for NaCl and KCl which are thought the be the most abundant salt species on Europa's leading hemisphere.

An exemption are hydrated states of these salt species which usually display distinct absorption features in the infrared range. But hydrated salts are not stable and dehydrate due to temperature and photolysis. A profound knowledge of related timescales is crucial for the understanding of Europa's surface history.

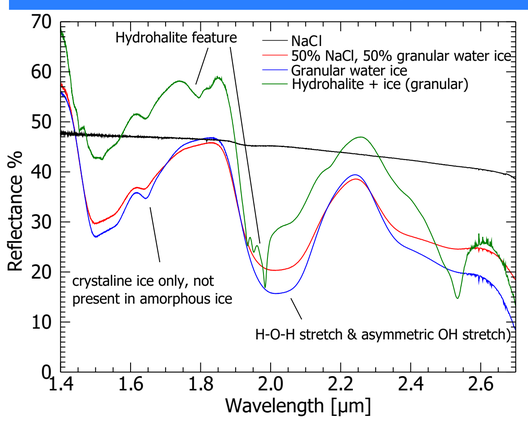
If features of hydrated salts were found by Europa clipper, they would indicate a relatively young terrain and recent resurfacing processes, such as plume particle depositions or frozen liquid outflows from the subsurface ocean or brine inclusions within the crust.



Methodology

Our laboratory measurements use passive near-infrared **reflectance spectroscopy** in the 1.4-7.0µm spectral range (Thermo Nicolet 6700 FTIR; Pike Tech DiffusIR). This configuration is comparable to spacecraft remote sensing with imaging spectrometers in terms of observation geometry and spectral resolution but differs in spatial resolution and SN-ratio. Laboratory measurements on mm-sized samples are performed at pressures of a few mtorr and temperatures in the 100-235K range.

(Near) Infrared - Hydration

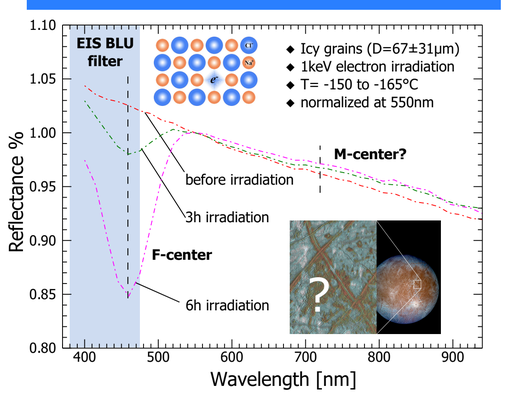


- only hydrated states of NaCl detectable
- Accessible in remote sensing
- Spectral range covered by the Mapping Imaging Spectrometer for Europa (MISE)

Anhydrous sodium chloride is spectrally flat across the visible and infrared wavelength range, while its hydrated state (Hydrohalite) shows distinct absorption features in the near infrared reflectance spectrum.

A mixture of 50% water ice and 50% NaCl is spectrally almost indistinguishable from pure water ice

Visible - Color centers

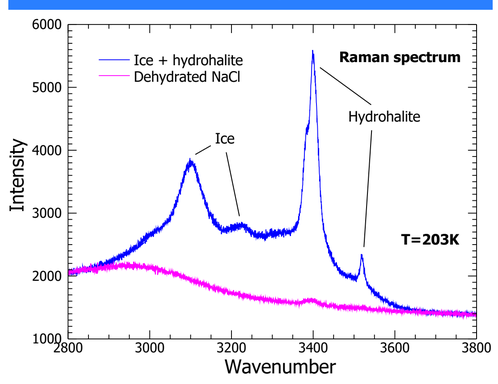


- Accessible by remote sensing and ground based observations
- Partially covered by the BLU filter on the Europa Imaging System (EIS)

What are color centers?

Color centers are a crystallographic defect where the anion (Cl^-) is replaced by an unpaired electron. They are formed by **electron bombardment** or **UV irradiation**. In case of NaCl it leads to absorptions at 460nm (F-centers) and 720nm (M-centers). This mechanism is a candidate for the formation of reddish-yellow linae on Europa but would be associated with 'older' terrain since only dehydrated salt are sensitive to this mechansim.

Raman - Hydration



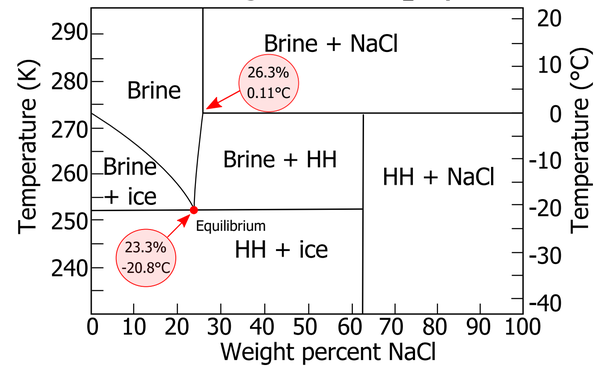
- hydrated states only
- clear chemical determination
- in-situ only, no remote sensing
- Europa lander

Hydrohalite

Sodium chloride dihydrate ($NaCl{\cdot}2H_2O$), also known as **hydrohalite** (HH) is selected as candidate material for our study since it is the only hydrated state of sodium chloride that can exist under Europa pressure and temperature conditions. Hydrohalite forms below 0.11°C under different NaCl concentrations. All our samples were produced with saturated brines.

Hydrohalite is found on earth under very rare conditions such as in lake bottom sediments in Antarctic dry valleys or isolated Siberian saline lakes during winter.

Phase diagram of Na-Cl-H_2O system



Key question:

How long can hydrohalite survive on Europa's surface before it gets dehydrated? This knowledge sets a maximum surface age in case of hydrohalite detection.

Goal of reserach

The main idea of this research is to build up laboratory catalog to quantifiy and interpret remote sensing data collected by the Europa clipper mission, especially from the MISE-instrument (**M**apping **I**maging **S**pectrometer for **E**uropa).

Experimental scenarios

We focus our experimental setup of icy samples on two distinct scenarios of exposition mechanisms that are potentially present on Europa:

1. Effusive flow from the subsurface ocean or brine pockets within the ice crust through cracks, leading to compact slab ice depositions.
2. Vapor driven plumes, similar to Enceladus, leading to porous accumulations of small flash frozen grains

First results

From our preliminary results it seems evident that the efficiency of hydrohalite-crystal formation (i.e. the hydration) is significantly reduced in case of flash freezing mechanisms, a significant portion of NaCl is embedded in a non-hydrated state, leaving more H_2O-ice in the sample.

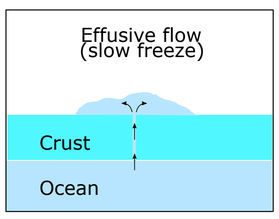
Granular ice dehydrates at least one order of magnitude faster than compact slabs, this effect might result form different volume-to-surface ratio.

Future work to do

Systematically add ultraviolet radiation to the experiments, investigate wavelength effects

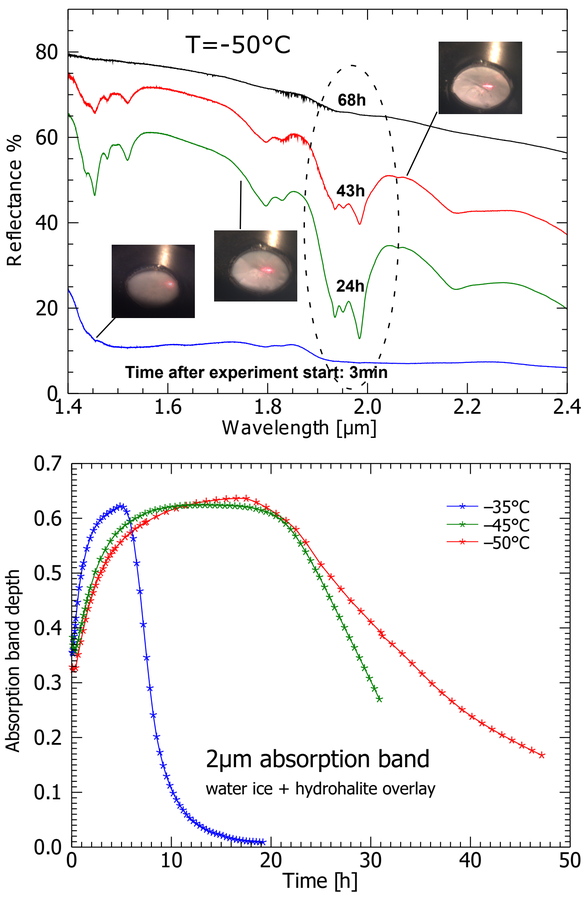
Dehydration kinetics

Slab ice

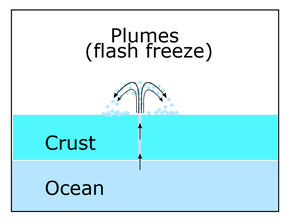


Long photon pathlength in the begining, absorption dominated.

Hydrohalite is embedded in ice matrix and gets exposed by sublimation of the surface layer.

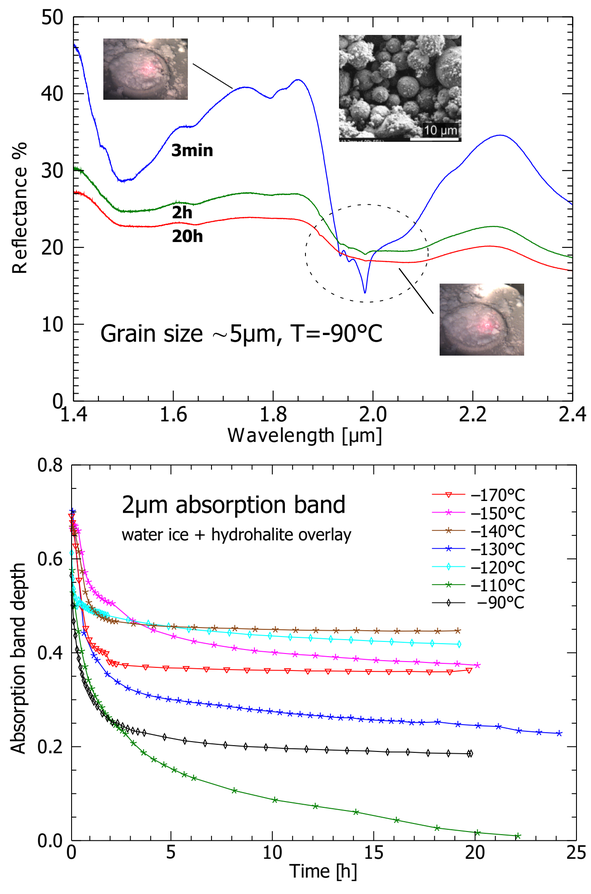


Granular ice



Very limited optical path-length, scattering dominated.

Hydrohalite formation is not efficient in fast freezing process. Excess water ice remains after dehydration.



Take home message:

- Hydrated salts can't survive on Europa's surface over long timescales, regardless of irradiation dose. They must be associated with cryovolcanic resurfacing processes
- The physical structure of frozen brines plays a crucial role for the dehydration timescales of hydrated salt minerals. Plume depositions are less likely to contain hydrated salts since the dehydration is faster and hydration is less efficient in flash-freezing processes

National Aeronautics and Space Administration

Jet Propulsion Laboratory
California Institute of Technology
Pasadena, California

www.nasa.gov

Copyright 2019. All rights reserved.

Poster No. P-10

Photopolymerization of HCN/HC_3N mixed ice to produce HCN-containing tholins

Stephanie McKean[1], Benjamin Fleury[1], Murthy S. Gudipati[1], and Isabelle Couturier-Tamburelli[2]

[1]Section 322, Jet Propulsion Laboratory, California Institute of Technology
[2]Aix-Marseille Université

National Aeronautics and Space Administration

Overview

HCN and HC_3N are the major atmospheric nitriles of Saturn's moon Titan. They are thought to participate in the formation of the condensed ices and photopolymerized aggregates that comprise Titan's haze layers. Laboratory analogues of haze particles are called "tholins".

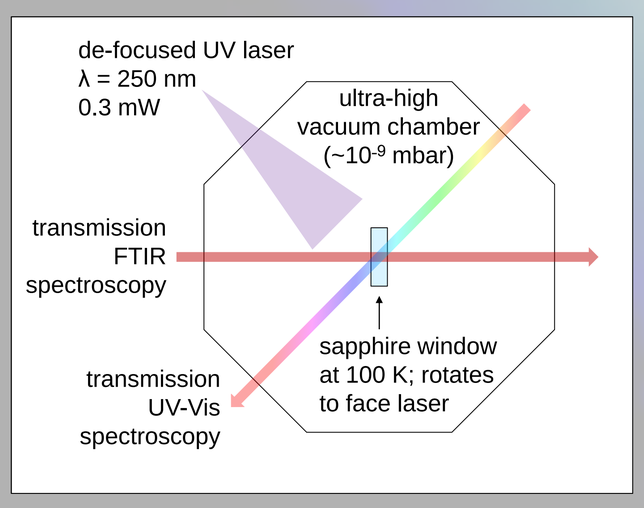
- In the condensed ice form, both molecules readily polymerize when exposed to ultraviolet (UV) light
- HC_3N ice photopolymerizes with UV light >300 nm. However, HCN ice requires <230 nm to photopolymerize
- Polymers aggregate and fall to Titan's surface, collecting more material and undergoing further photochemical processing on the way
- Only 10% of incident sunlight reaches Titan's surface, and shorter wavelengths are attenuated in the upper atmosphere
  - *Polymerization can be altitude-dependent*
- Amino acids and nucleobases have been derived from these polymers when in contact with oxygen-rich species
  - If HCN can be incorporated into photopolymers over a wider range of UV wavelengths, then more pre-biotic precursors can form on Titan's surface

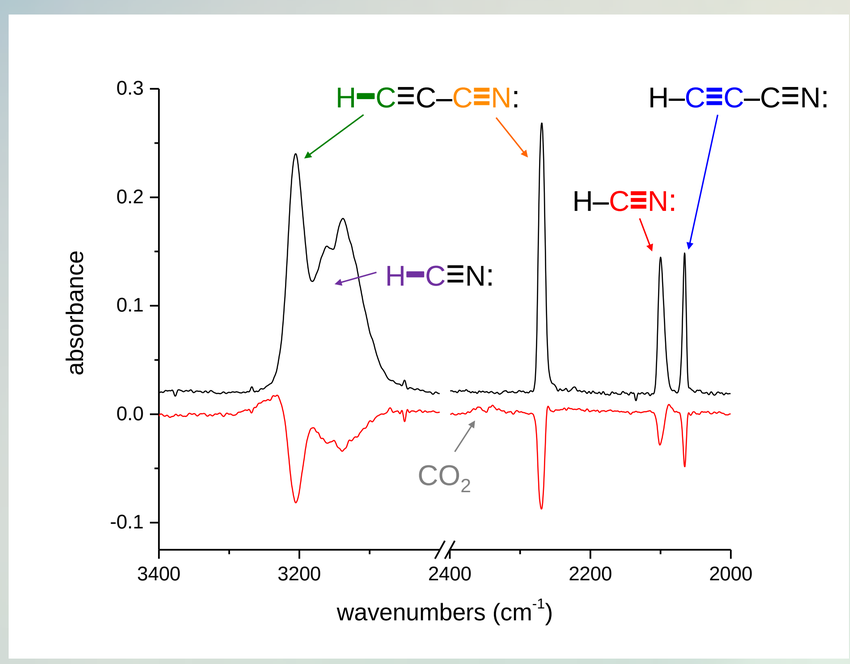
If HCN/HC_3N mixed ice is irradiated with 250-nm laser light, will HCN be incorporated into the polymer, despite being transparent to the radiation?

Experimental

HCN and HC_3N gases are condensed on a cold (100 K) surface and irradiated with a defocused laser to induce polymerization.

- Changes in the mixed ice are monitored using transmission Fourier-transform infrared spectroscopy (FTIR) and transmission UV-Visible (UV-Vis) spectroscopy
- Material that desorbs during irradiation and when warming to room temperature are monitored by a quadrupole mass spectrometer (not shown).

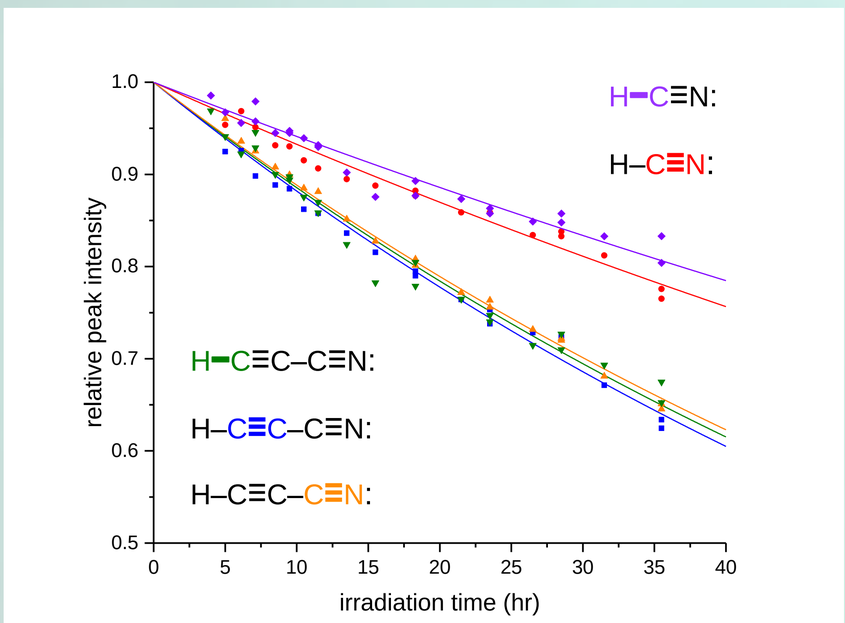




The initial absorbance spectrum of a 1:2 ratio of HCN and HC_3N as mixed ice (black; offset for clarity) is used to calculate the differential absorbance after 35.5 hours of 250-nm irradiation (red). Absorbance above zero indicates that polymeric material was added, and negative peaks indicate loss of material.

Integrate negative peaks of the differential spectra

Normalize the values relative to initial intensity

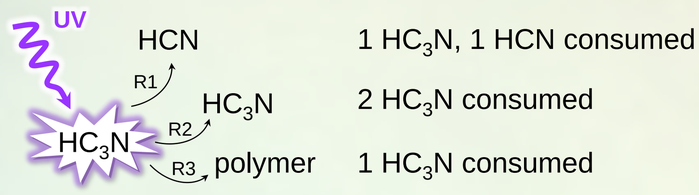


Normalized decrease over time of HCN and HC_3N stretching bands located at 2066 cm^{-1}, 2100 cm^{-1} (HCN), 2270 cm^{-1}, 3136 cm^{-1} (HCN), and 3200 cm^{-1}, obtained by integrating the peaks of the differential absorbance spectra. Best-fit lines are exponential decays of the form $y=\exp[-cx]$ where c is the decay rate.

Results and Analysis

FTIR peaks for HCN and HC_3N both decayed exponentially with irradiation time.

- HCN has a decay rate of 0.0065 ± 0.0005 hr^{-1}
  HC_3N has a decay rate of 0.0122 ± 0.0004 hr^{-1}
- There are 2 HC_3N molecules for every HCN molecule. If an excited HC_3N molecule were equally likely to react with HCN (R1) or HC_3N monomers (R2), the decay rates would have a ratio of 1:≥3 instead of 1:2



- The rate of HC_3N consumption by reaction with existing polymer cannot be quantified, so the 1:3 ratio is bounded

Excited HC_3N preferentially reacts with HCN over HC_3N by a factor of ≥ 2

- UV-Vis spectra showed that over time, more light is absorbed across the 200-1050 nm spectrum, but primarily from 200-500 nm
  - This is consistent with production of a colored product. Pure HC_3N polymer is dark brown and HCN polymer is black
  - Black residue was seen on the window

The product of these reactions is a copolymer of HCN and HC_3N

Impact

In the solid phase, absorption of 250-nm radiation by HC_3N causes it to react with HCN and itself, forming a polymer that incorporates both molecules.

- HCN can polymerize even if it is not directly excited (but indirectly photoactivated)
- HCN can be reactive in the atmospheric region of Titan where it condenses with other molecules, even though it is transparent to the solar radiation at that altitude (<200 km)
- This significantly increases the amount of polymer that can form and the amount of pre-biotic molecules that may form once the haze particles reach Titan's surface and interact with oxygen-rich species such as water-ice

Future

- Determine the rate of consumption for HC_3N irradiated with 250-nm light in the absence of HCN and in a 1:1 ratio for comparison to the results presented here
- A more sensitive FTIR detector is now available and may be able to resolve the peaks of species formed during irradiation

Acknowledgments
This work is conducted at JPL under a NASA Solar System Working (SSW) Grant "Photochemical Processes in Titan's Atmospheric Ice and Aerosols" to Murthy S. Gudipati.

National Aeronautics and Space Administration
Jet Propulsion Laboratory
California Institute of Technology
Pasadena, California

www.nasa.gov

Copyright 2019. All rights reserved.

Poster No. P-11

Background image: https://apod.nasa.gov/apod/ap041028.html

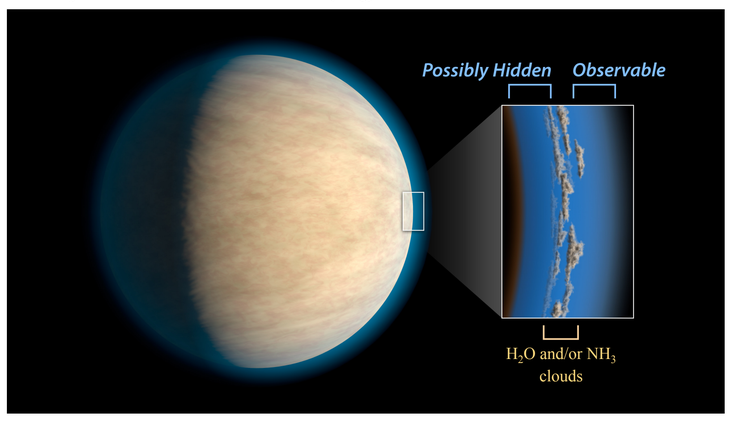
National Aeronautics and Space Administration

ExoReL: a new frontier for reflection spectroscopy

Author: Mario Damiano (JPL, 3262)
Renyu Hu (JPL, 3262)

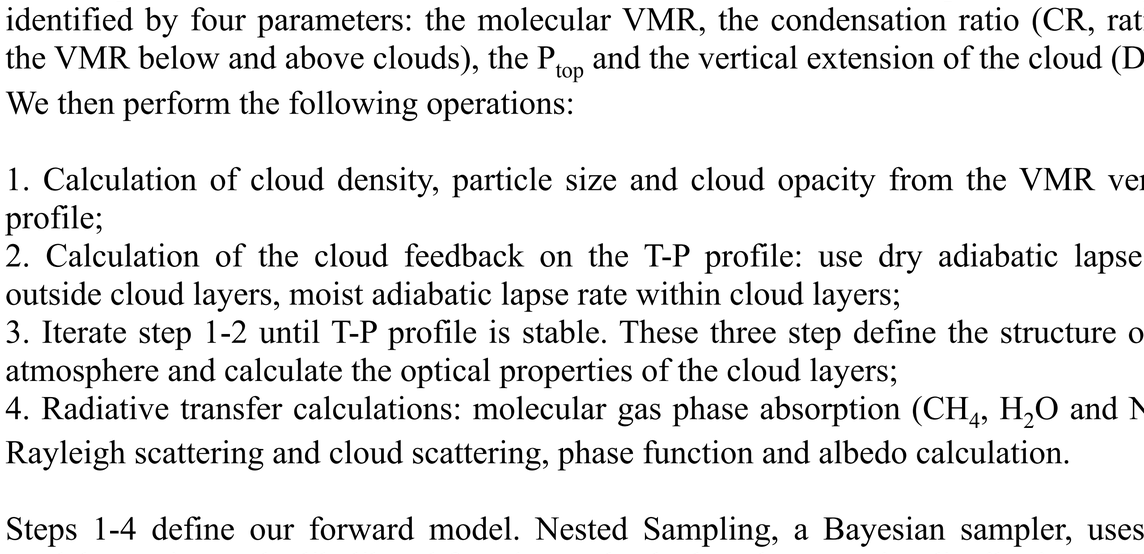
Summary

The high-contrast imaging technique will provide insights into those planets orbiting far away from their host star (distance > 1 AU) so that their atmospheric temperature is low enough to show different chemical and dynamical behavior (e.g. condensation mechanism, cold trap effects, etc.). Future space missions, such as WFIRST, LUVOIR, and HabEx, are meant to observe the light reflected by the exo-planetary atmosphere. The reflection spectrum is a glimpse into the structure of atmospheric condensates [1,2]. Assuming an atmospheric elemental abundance the same as the Sun, giant exo-planets may have ammonia, water, or silicate clouds in their atmospheres. Whether there exist clouds is the primary factor that controls the appearance of an exoplanet. These observations, mostly conducted in the optical wavelength, may probe the molecular signatures of methane, ammonia and water vapor as well as clouds properties [3,4,5,6].



Objective

By focusing on cold gaseous planets, the goal of this work is to build a Bayesian inverse retrieval framework for reflection spectra to determine water and ammonia clouds physical properties and concentration of H_2O, NH_3, and CH_4 in the atmosphere. Moreover, differently from previous works on the subject [7,8], here, clouds are not referred in general, we gave them a chemical identity. In the forward model, a water cloud is different from an ammonia cloud [3,4,5,6].

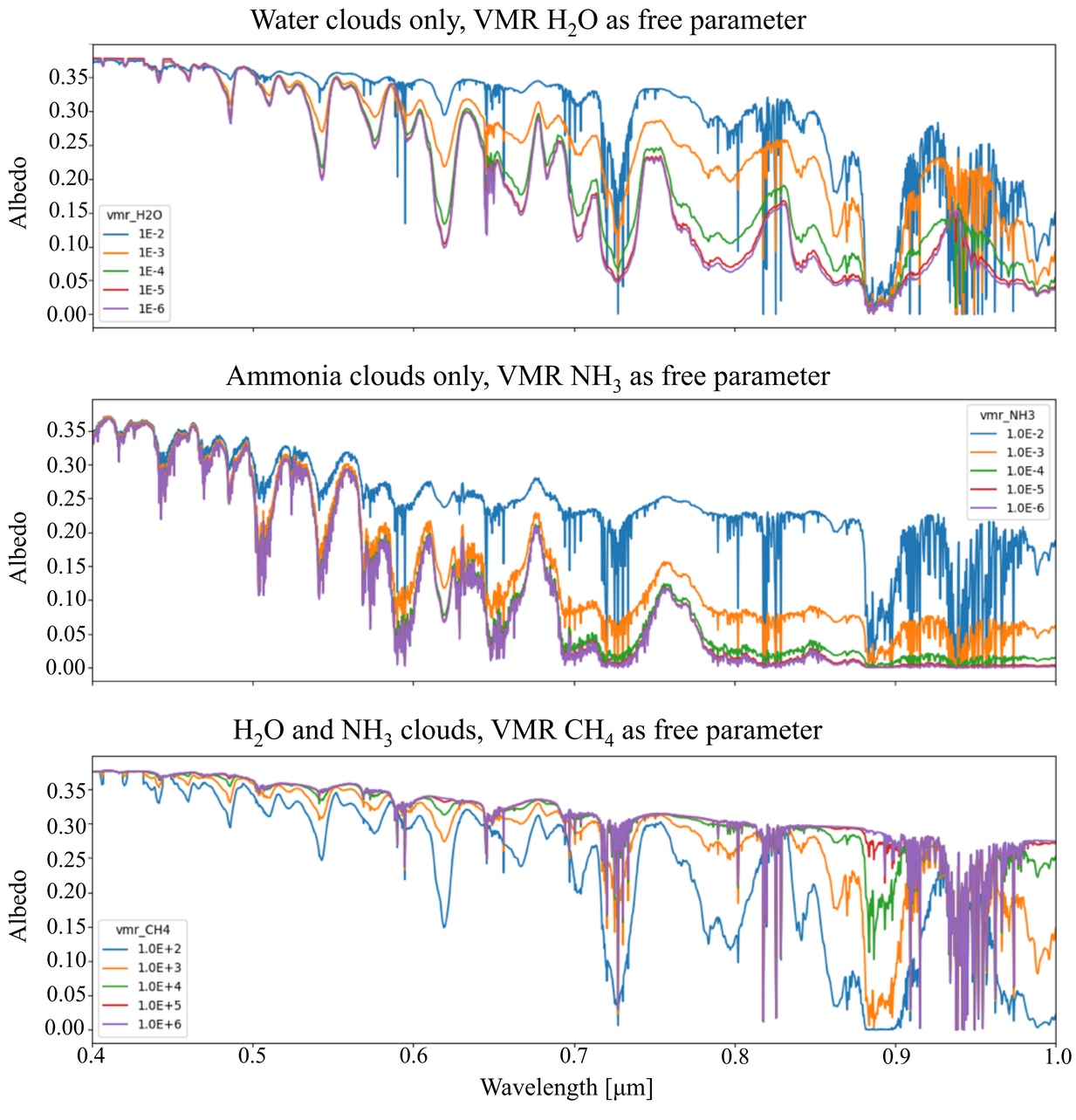


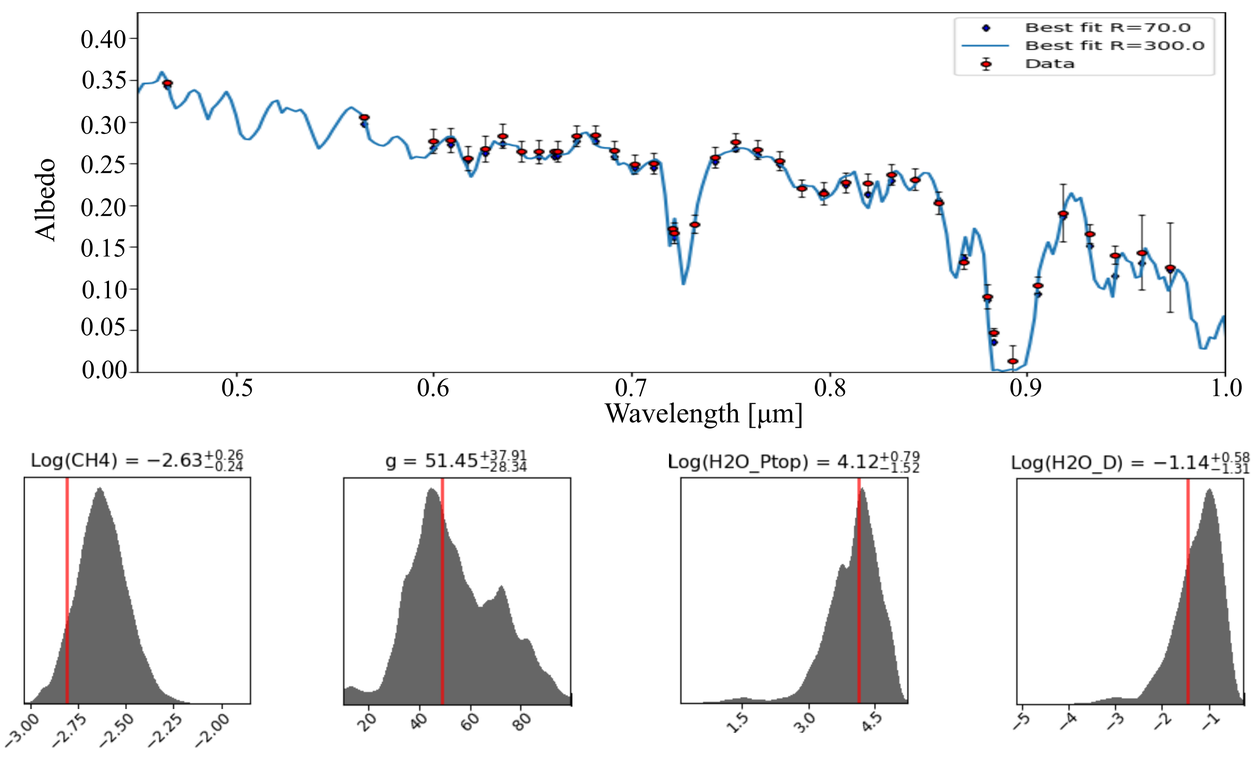
Methodology

The free parameters space comprises the gravity (g), the VMR of methane and two VMR vertical profiles: one for water and one for ammonia. Each of these profiles is uniquely identified by four parameters: the molecular VMR, the condensation ratio (CR, ratio of the VMR below and above clouds), the P_{top} and the vertical extension of the cloud (D_{cld}).
We then perform the following operations:

1. Calculation of cloud density, particle size and cloud opacity from the VMR vertical profile;
2. Calculation of the cloud feedback on the T-P profile: use dry adiabatic lapse rate outside cloud layers, moist adiabatic lapse rate within cloud layers;
3. Iterate step 1-2 until T-P profile is stable. These three step define the structure of the atmosphere and calculate the optical properties of the cloud layers;
4. Radiative transfer calculations: molecular gas phase absorption (CH_4, H_2O and NH_3), Rayleigh scattering and cloud scattering, phase function and albedo calculation.

Steps 1-4 define our forward model. Nested Sampling, a Bayesian sampler, uses this model to estimate the likelihood function and calculate the posterior distribution (PDF) of the input free parameters.





Results

- Determination of cloud structure (position, extension, density);
- Identification of different molecular condensates (water or ammonia clouds);
- Indirect determination of the planetary radii from the gravity;
- Detection and quantification of the atmospheric concentration of CH_4;
- Indirect quantification of VMR of water and ammonia.

National Aeronautics and Space Administration
Jet Propulsion Laboratory
California Institute of Technology
Pasadena, California

www.nasa.gov

Copyright 2019. All rights reserved.

References:
[1] Marley, M.S. et al. (1999), ApJ, 513, 879.
[2] Seager, S. et al. (2000), ApJ, 540, 504.
[3] Hu, R. et al. (2012), ApJ, 761, 166.
[4] Hu, R. el al. (2013), ApJ, 769, 6.
[5] Hu, R. et al. (2014), ApJ, 784, 63.
[6] Hu, R. (2014), ArXiv:1412.7582.
[7] Lupu, R,E. et al. (2017), AJ, 152,217.
[8] Batalha, N,E. et al. (2019), ArXiv:1904.09355.

Poster No. P-13

Reconnection signatures at Saturn's Magnetopause: FTEs and TCRs

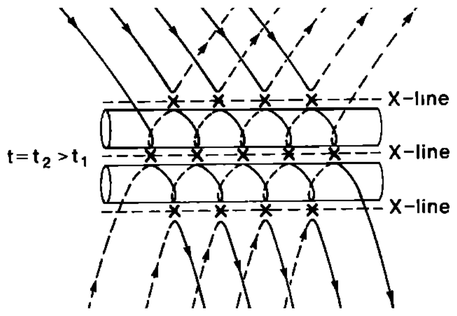
Jamie M. Jasinski[1,*], Weijie Sun[2], Neil Murphy[1], James A. Slavin[2], & Andrew J. Coates.[3]

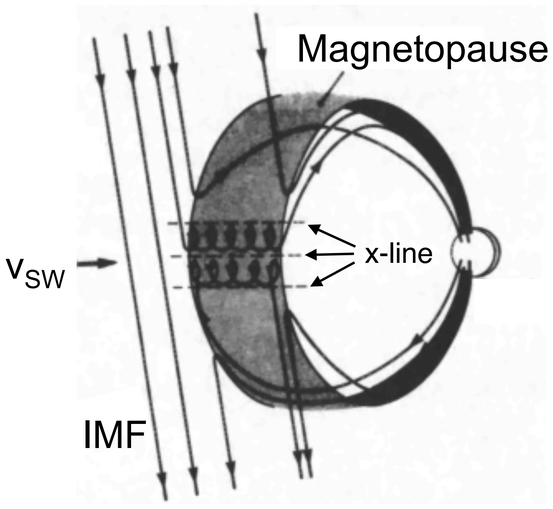
1. NASA Jet Propulsion Laboratory, California Institute of Technology, CA, USA; 2. Dept. of Climate and Space Sciences and Engineering, University of Michigan, MI, USA; 3. Mullard Space Science Laboratory, Dept. of Space and Climate Physics, UCL, UK.
* email: jasinski@jpl.nasa.gov

Why is this important?

- These magnetic structures are important to study at Saturn because they are generated by multiple x-line reconnection at the magnetopause, which is rare at Saturn.

- We can understand more about reconnection at Saturn, as well as understand more about reconnection physics by studying it at a different environment (other than at Earth and Mercury, where reconnection drives the magnetosphere).

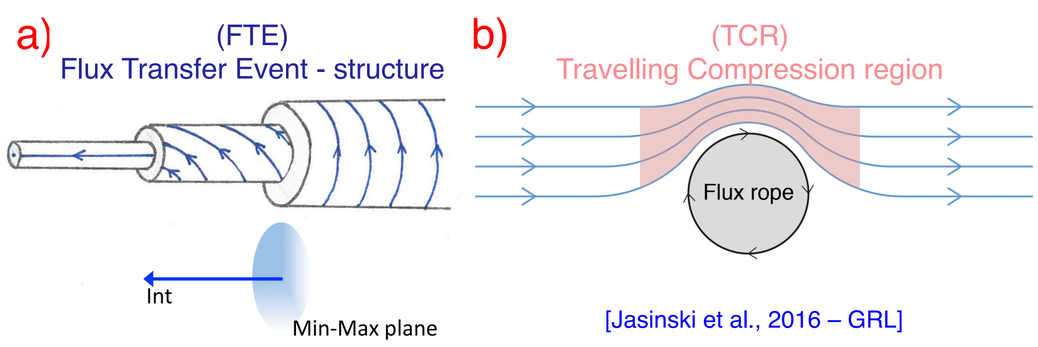




[Lee and Fu, 1985]

What are we looking for?

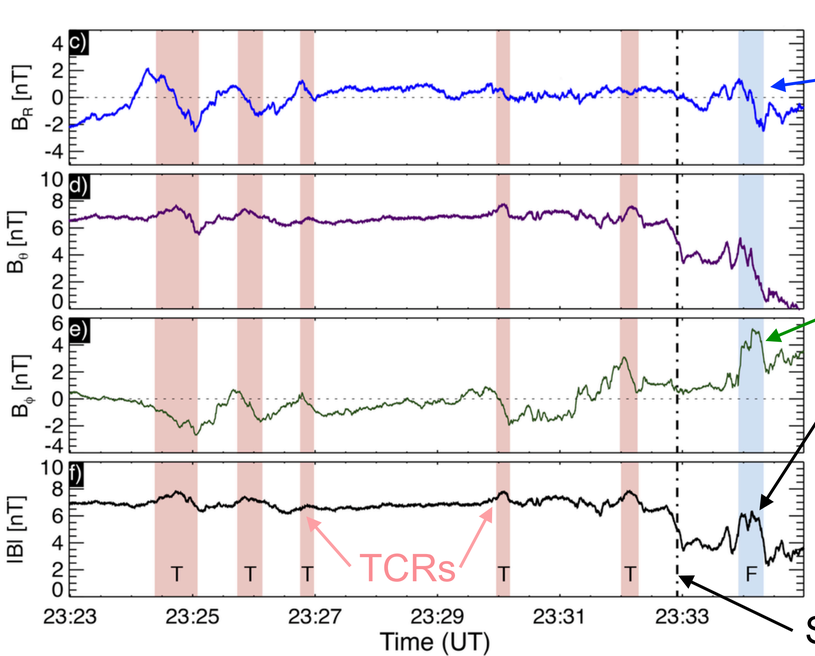
- a) The FTEs twisted magnetic field structure produces a bipolar signature observed in the magnetic field measurements, as well as an increase in magnetic field strength at the centre of the FTE.



[Jasinski et al., 2016 – GRL]

- b) If the spacecraft does not cross through the FTE, but passes near the edge, then a travelling compression region (TCR) is observed due to the draping of the magnetic field around the flux rope (red shading above).

First detection: *Jasinski et al.*, (2016)



FTE Bipolar signature

Increase in core direction of FTE

And energisation in plasma (not shown here).

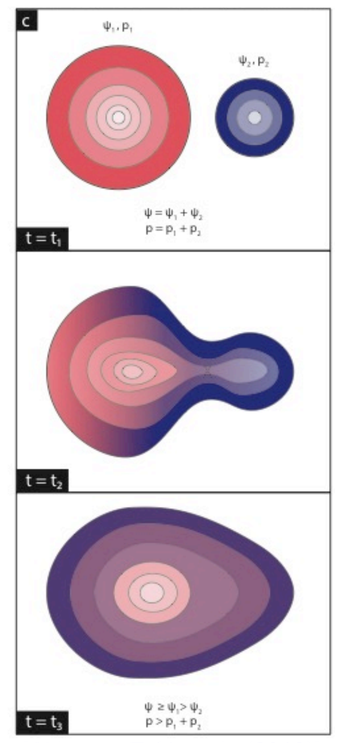
Saturn's magnetopause

What's happening at Saturn?

Three ways to grow an FTE:
a) Adiabatic expansion
b) Continuous reconnection (most common at Earth)
c) Secondary reconnection (coalescence)

At Saturn, reconnection rates are low, therefore mechanisms to grow an FTE reduced. Is this why previous studies "miss" them?

Small FTEs more likely to be common at Saturn.



[Akhavan-Tafti et al., (2019)]

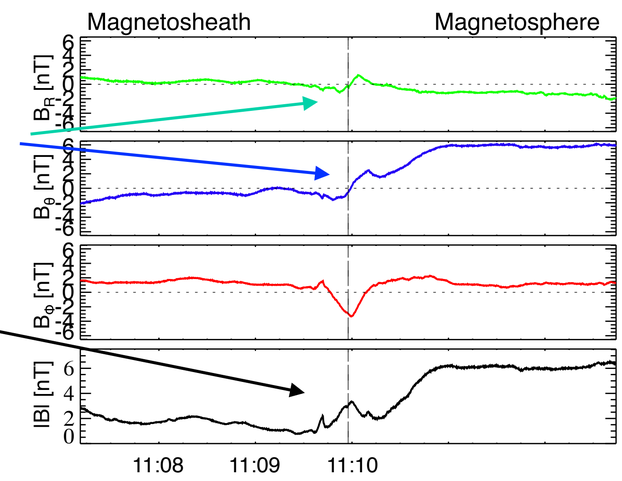
The Algorithm

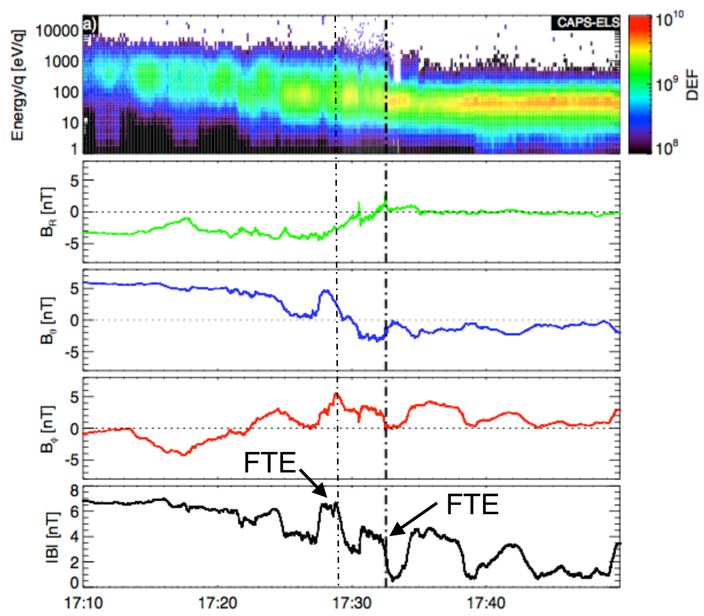
At the Magnetopause:

Identify bipolar signatures in B_R, B_θ or B_ϕ.

Also identify peak in |B| which is >0.5 ΔB

Has been used to identify FTEs at Mercury.





Mixed plasma of magnetospheric and magnetosheath plasma

First test run identified 5 new FTEs and 18 TCRs at the magnetopause in the MAG data.

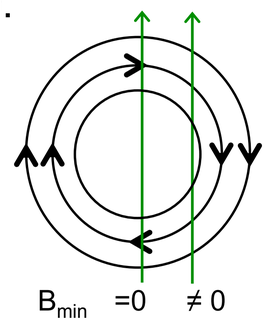
We will adjust parameters of the algorithm and rerun after initial analysis.

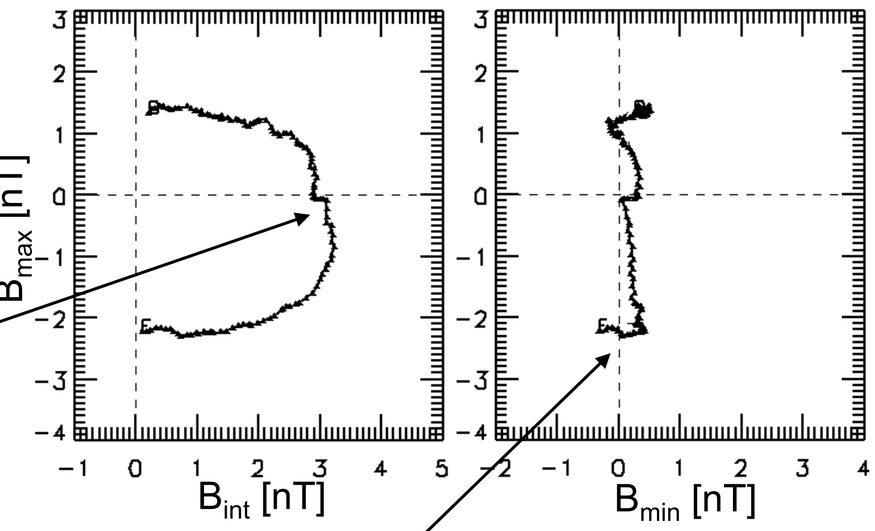
MVA analysis

Minimum variance analysis (MVA) helps us understand structure and the orientation of FTE.

Bipolar signature in B_{max}

Core is in the B_{int} direction.





B_{min} is close to 0
This means Cassini crossed near the flux rope core.

P – 14

National Aeronautics and Space Administration

Atmospheric tomography: A valuable asset for current Mars orbiter and future planetary CubeSat missions

Author: Gregor Moeller (335G)
Co-Authors: Chi O. Ao (335G) and Anthony J. Mannucci (3350)

Conclusion

In a future mission scenario, a series of CubeSats is injected into a low Mars orbit, as payload on a larger orbiter. Based on the established constellation, planetary and cross-link occultations are obtained with a geometry suited for tomography processing. Tomography principles applied to Mars Reconnaissance Orbiter measurements have demonstrated the potential for resolving horizontal gradients of pressure and temperature in the lower Martian atmosphere. **With the proposed CubeSat constellation, global sampling of time-varying phenomena will become possible with high spatial and temporal resolution.**

Problem statement

Current Mars orbiters like Mars Odyssey, Mars Reconnaissance Orbiter (MRO) or MAVEN are in sun-synchronous or highly elliptical orbit. Such orbits are not very well suited for sampling the diurnal cycle. In addition, distinct horizontal gradients in atmospheric pressure and temperature cannot be resolved with existing radio occultation processing strategies.

CubeSat constellation

The suggested constellation is based on **four CubeSats in low Martian orbit**, separated by 120sec (see Table1 for orbital elements). Each CubeSat is equipped with deployable antenna features for signal relay in X-band and UHF band.

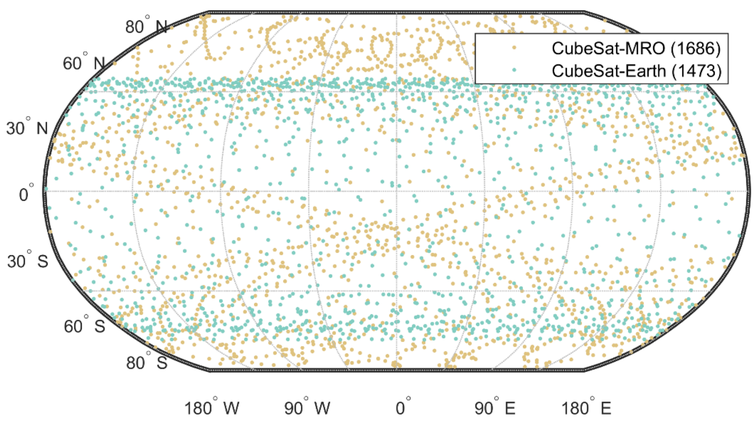


Figure2: Expected radio occultation events between CubeSats, MRO and Earth within a precession cycle of 67 sols

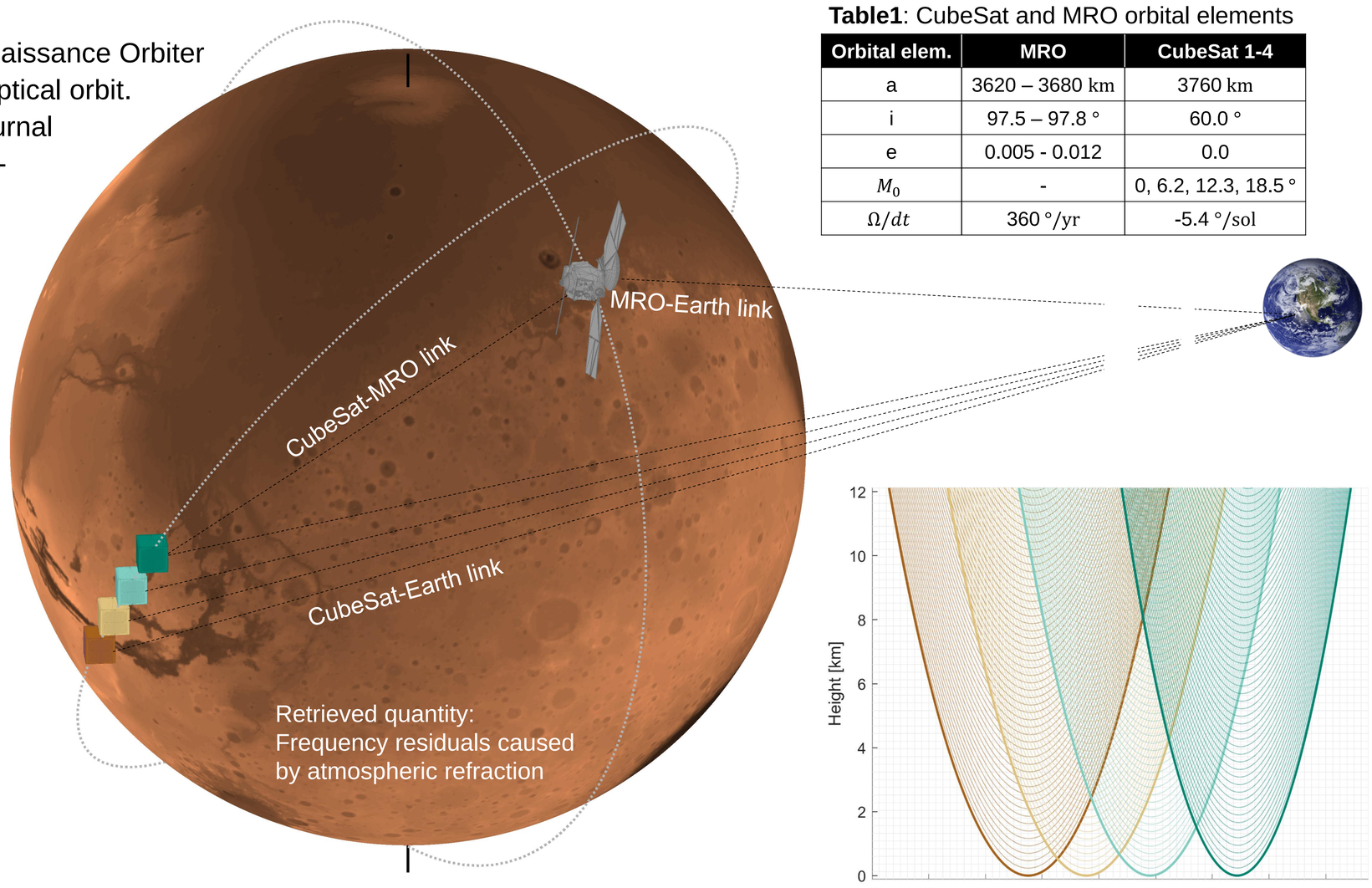


Figure1: CubeSat constellation and resulting radio occultation links to Earth and MRO (links to other orbiters are possible but have not be analyzed yet)

Table1: CubeSat and MRO orbital elements

Orbital elem.	MRO	CubeSat 1-4
a	3620 – 3680 km	3760 km
i	97.5 – 97.8 °	60.0 °
e	0.005 - 0.012	0.0
M_0	-	0, 6.2, 12.3, 18.5 °
Ω/dt	360 °/yr	-5.4 °/sol

Figure3: Ray-path geometry through the lower Martian atmosphere as expected for each radio occultation event in Figure2

Methodology: Atmospheric tomography

In order to apply tomography principles to radio occultation measurements:

(1) the two-way **frequency residuals** (df) are converted into phase delays (dL)

$$dL = \sum_i dL(i) + \Delta dL(i) \quad \text{with } \Delta dL = df/(1 + f_t/f_r) \cdot \mathrm{c/f_r} \cdot \mathrm{dt}$$

where f_t and f_r are the transmitted and received frequency, respectively

(2) the RO signal paths through the voxel model are reconstructed by 3D **ray-tracing** through an a priori model of refractivity

(3) the converted phase delays are introduced into the **tomography** system as follows: $N = \mathbf{A}^{-1} \cdot dL$, where matrix $\mathbf{A}$ contains the partial derivatives of the phase delays with respect to unknowns (N), i.e. the traveled distances in each voxel. The resulting equation system is solved for refractivity by weighted least squares techniques, combined with truncated singular value decomposition methods (TSVD).

Expected Results: 2D temperature fields

For technique demonstration, MRO radio occultation (RO) and Mars Climate Sounder (MCS) measurements were processed together using tomography principles. It allows for reconstruction of the temperature distribution in the lower atmosphere with a spatial resolution of about 200km x 0.7km. However, from the suggested CubeSat constellation, more information about the lower atmospheric layers are expected with a 10x better horizontal resolution.

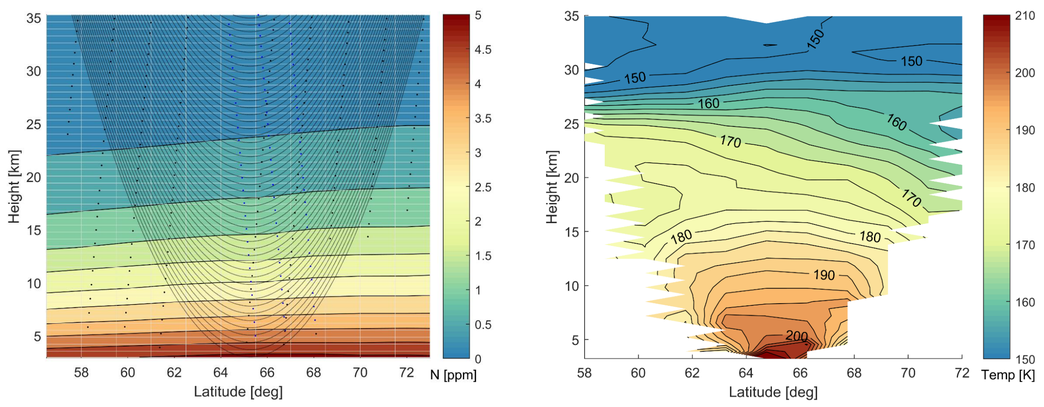


Figure4 left: Co-located RO/MCS observation geometry for a single RO event in Dec 2011. This includes the RO ray paths (black lines), the coordinates of the observed MCS profiles (black/blue dots) and the boarders of the tomography voxel model (white lines)

Figure4 right shows the 2D temperature field as obtained by combined processing of RO and MCS data using tomography principles

National Aeronautics and Space Administration

Jet Propulsion Laboratory
California Institute of Technology
Pasadena, California

www.nasa.gov

Copyright 2019. All rights reserved.

References

Capderou M. and Forget F.: Optimal orbits for Mars atmosphere remote sensing, Planetary and Space Science, https://doi.org/10.1016/j.pss.2004.03.006, 2019

Moeller G., Ao C. O., Yang Y.-M., Mannucci A. J.: Analysis of the lower Martian atmosphere by combined processing of radio occultation and Mars Climate Sounder measurements, doi:10.13140/RG.2.2.28506.80322, Poster EGU General Assembly, Vienna, Austria, 2019

Williamson W. R., Ao C. O., Mannucci A. J.: Radio occultation mission to Mars using cubesats, Presentation International Conference on Mars Aeronomy, 15-19 May 2017, Boulder, Colorado, USA

Poster P-17

National Aeronautics and Space Administration

Observability of Venus' torque balance

Author: Anton I. Ermakov (392R)

Ryan S. Park (392R), Bruce G. Bills (3224), Thomas Navarro (UCLA), Gerald Schubert (UCLA), Krzysztof Gorski (3268)

1. Introduction

- The present slow retrograde rotation of Venus has long been hypothesized to be due to a torque balance [e.g.: 1].
- We constrain the net torque on Venus, which depends on the atmospheric thermal tide and solid body gravitational tide.

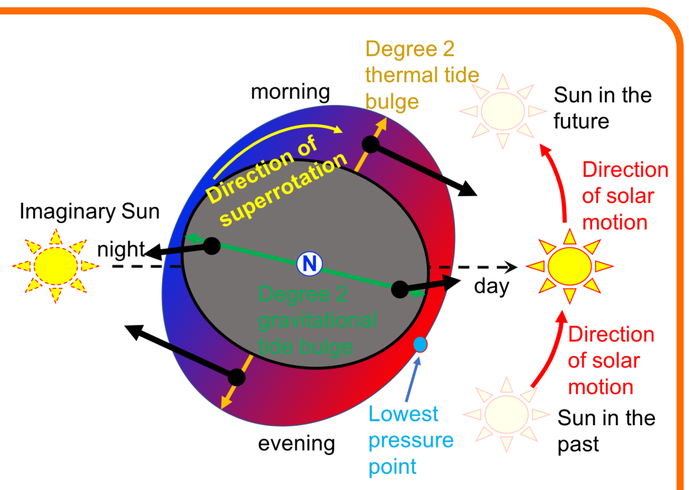


Fig. 1: Sketch of Venus tidal bulges.

Our goals are:

- To characterize the testability of the torque balance hypothesis via measurements of Venus gravity.
- To characterize the temporal variability of the net torque from the atmosphere using a global circulation model.
- We show that the net torque is related to the time variation of the degree 2 gravity terms. Even though the net torque can average to zero over a long-time scale, the sporadic mass motion in the atmosphere results in a non-zero instantaneous torque.
- In addition, equating the torque from the atmosphere to the solar gravitational torque, we find the quality factor *Q*, related to the dissipation within Venus, required to maintain the torque balance.

2. Theory

- We compute the atmospheric contribution to gravity coefficients ($\delta\bar{C}^a_{nm}, \delta\bar{S}^a_{nm}$) by compressing atmosphere onto a thin layer:

Gravitational potential of the atmosphere; Venus mass

$$U_a = \frac{GM}{r}\sum_{n=0}^{\infty}\sum_{m=0}^{n}\left(\frac{R}{r}\right)^n (\delta\bar{C}^a_{nm}\cos m\lambda + \delta\bar{S}^a_{nm}\sin m\lambda)\bar{P}_{nm}\sin\varphi\,.$$

Associated Legendre functions

$\delta\bar{C}^a_{nm}$ and $\delta\bar{S}^a_{nm}$ can be found from the surface pressure spherical harmonic coefficients δC^P_{nm} and δS^P_{nm}:

$$\{\delta\bar{C}^a_{nm}, \delta\bar{S}^a_{nm}\} = (1+k^{load}_{nm})\frac{4\pi R^2}{gM}\frac{\{\delta C^P_{nm}, \delta S^P_{nm}\}}{(2n+1)}$$

Loading Love number; Surface gravity; Spherical harmonic coefficients of pressure anomaly

- Due to Venus' non-spherical gravity field, the Sun exerts torque on Venus:

$$\tau^{grav}_{\odot\to(a+b)} = M_\odot \vec{r}\times\vec{\nabla}U_{a+b}$$

Subscript "a" for atmosphere; Subscript "b" for solid body

- Torque on atmosphere (a) may balance the torque on the solid body (b):

*Total torques are dominated by degree 2 torques

$$\tau_{\odot\to a} = \frac{\sqrt{15}GMM_\odot R^2\delta\bar{S}^a_{22}}{a^3}$$

in Sun-fixed frame; orbit semimajor axis

$$\tau^{grav}_{\odot\to b} = \frac{3}{2}GM^2_\odot\frac{R^5}{a^6}\frac{k^{tidal}_2}{Q}$$

Tidal Love number; Dissipation factor

- Given a Global Circulation Model (GCM) and measured value of k^{tidal}_2, we can find a condition on dissipation within Venus and loading Love number that would result in torque balance (see Section 5): $\tau^{grav}_{\odot\to a} + \tau^{grav}_{\odot\to b} = 0$
- Total torque (atmosphere + solid body) is $\propto \delta\bar{S}^{a+b}_{22}$ in Sun-fixed frame.

3. Data

- Fig 2. shows the RMS spectrum of different static and dynamic contributions to gravity.
- Static gravity field and Love number k^{tidal}_2 was observed by the Magellan spacecraft [2].

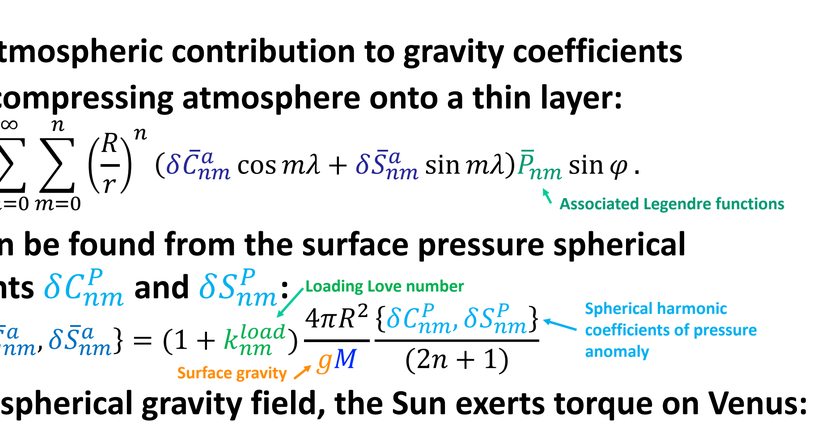


Fig 2. Amplitude spectra of static and dynamic contributions to Venus gravity. The shaded regions span from 5th to 95th percentile.

- *Institut Pierre-Simon Laplace* GCM was used to produce synthetic time-variable gravity due to Venus atmosphere [3].
- The GCM results show that the dynamic atmosphere of Venus creates a time-variable gravity (TVG) signal only a factor of 9 below the sensitivity of the existing Magellan data (Fig. 2).

4. Results

- Venus' atmospheric TVG is dominated by the thermal tide at a period of one Venus day (≈117 Earth days).
- Thermal tide is computed by averaging pressure in the Sun-fixed frame (Fig. 3).
- Using GCM surface pressure field, we get a torque balance condition: $Q\left(1+k^{load}_2\right) = 39.8$ (Fig. 4).
- Gravitational torque of Venus atmosphere is dominated by torque on the thermal tide bulge (Fig. 5).

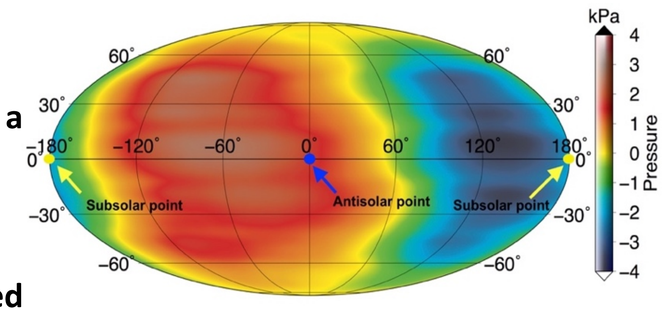


Fig. 3: Map of thermal tide pattern, in Sun-fixed frame. Midnight is on the prime meridian and noon is at either edge.

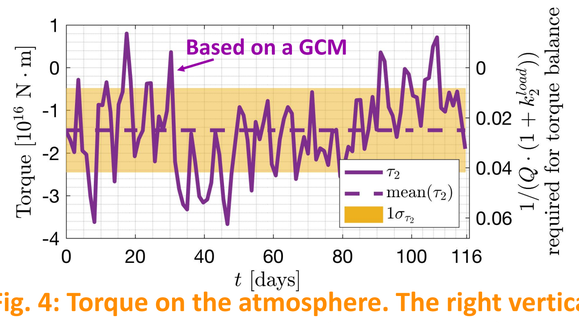


Fig. 4: Torque on the atmosphere. The right vertical axis shows the values of $1/\left(Q\left(1+k^{load}_2\right)\right)$ required to maintain torque balance.

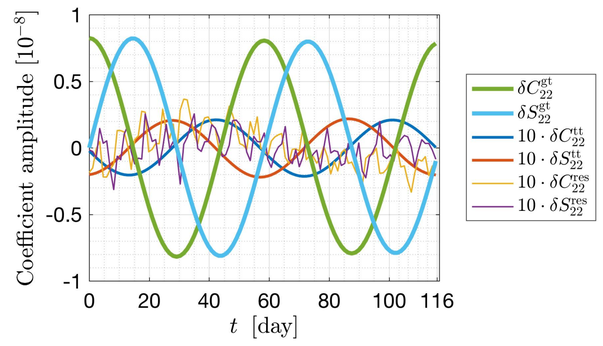


Fig. 5: Time series of degree 2 gravity coefficients. The subscript "gt" denotes the solid body tides. The subscript "tt" denotes the thermal tide in the atmosphere. The subscript "res" denotes the residual after modeled thermal tide was subtracted from the modeled atmospheric signal.

Table 1: The magnitudes of various static and dynamic gravity signals at Venus.

Type of gravity signal		RMS amplitude [mGal]
Static gravity	static solid body $\bar{g}$	887000
	static (averaged) atmosphere $\bar{g}_a$ (using GCM)	430
Dynamic gravity	gravitational tide on atmosphere	to be computed
	gravitational tide on solid body δg_{solid} [2]	0.024-0.025
	thermal tide δg_{tt} (using GCM)	0.004
	residual atmospheric signal δg_{res} (using GCM)	0.001 – 0.003

5. Conclusions

- Atmosphere of Venus creates a time-variable gravity signal a factor of 9 below the sensitivity of the existing Magellan gravity data [2].
- Therefore, the next mission to Venus with gravity mapping capability will likely be sensitive to Venus' atmospheric TVG.
- The degree 2 gravity terms of the thermal tide result in a torque on Venus' atmosphere. This torque is of the opposite sign than the torque due to gravitational solid body tide.
- The total torque is proportional to $\delta\bar{S}^{a+b}_{22}$ in the Sun-fixed frame that can be measured by solving for time-variable S_{22} is Venus-fixed frame.
- Using a GCM, we constrain $Q\left(1+k^{load}_2\right)$ required to maintain torque balance on Venus.
- Notice a trade-off between the loading Love number k^{load}_2 and dissipation factor Q in the torque balance equation!
- Venus' atmospheric TVG, if measured, would be highly complementary to lander measurements and remote sensing orbital data as it would provide a global insight into deep Venus' atmosphere. Our analysis will be helpful in connecting the GCM results and future gravity observations.

6. References: [1] Dobrovolskis, A.R. and Ingersoll, A.P., 1980. Icarus 41.1, pp 1-17; [2] Konopliv A.S. et al., 1999. Icarus 139.1, pp. 3-18; [3] Lebonnois, S. et al., 2016. Icarus, 278, pp. 38-51.

Poster P-17

National Aeronautics and Space Administration, Jet Propulsion Laboratory, California Institute of Technology, Pasadena, California, www.nasa.gov, Copyright 2019. All rights reserved.

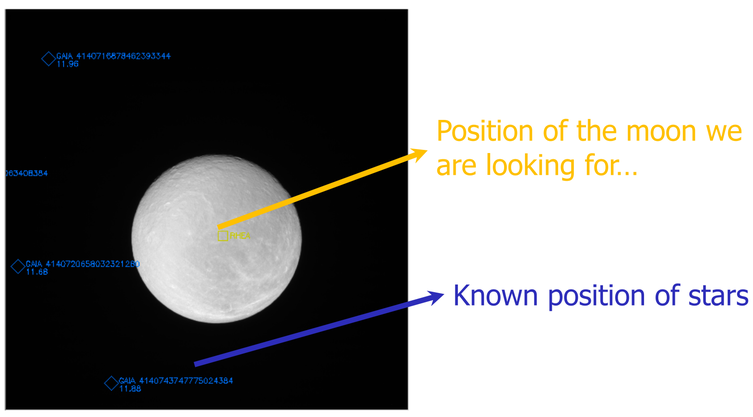
National Aeronautics and Space Administration

Astrometry unleashed: The Saturnian system

Authors: Valéry LAINEY (392)
Ryan PARK (392)

What is astrometry?

Astrometry is the discipline that aims at determining the position of celestial objects with the highest accuracy.



Typical measurement accuracy: few km!

Note: Saturn is more than 1.5 billion km away, and Saturn's moons, as well as the orbiter itself, are moving at several to few tens of km per second…

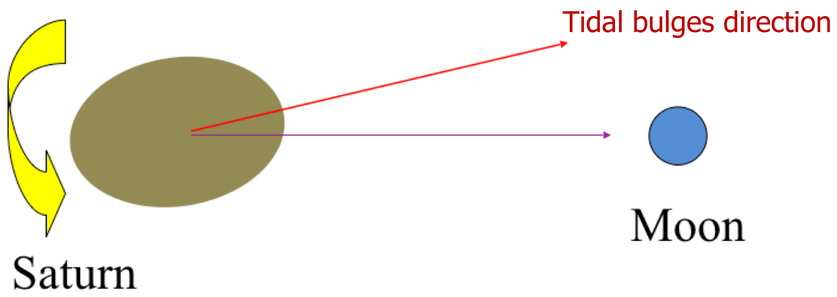
Why do we care even though Cassini is not there anymore?

Cassini mission was an immense success for JPL. Still, we have found some signatures in the orbits that we do not fully understand. This suggests that we are still missing a part of the physics at play… Hopefully, analyzing these signals may help answering the still extremely debated question: what is the age of the main moons and how did they form?

Saturn's moons carry a lot of physical information including:

- Interior mass distribution → formation process
- Tidal dissipation → long term evolution of the orbits

Example:



Tides raised on Saturn by one of its moons

Like an ice-skater is spinning faster when his or her arms are folded in, the Saturn's spin and the moons radial distance are linked. While friction arises inside Saturn associated with tidal deformation, its spin is decreasing and the moon's orbit is expanding.

Did you know?: The Earth's moon distance is increasing at about 3.8 cm/year because of the tides the Moon raises on our own planet.

National Aeronautics and Space Administration
Jet Propulsion Laboratory
California Institute of Technology
Pasadena, California

www.nasa.gov

Copyright 2019. All rights reserved.

Our method

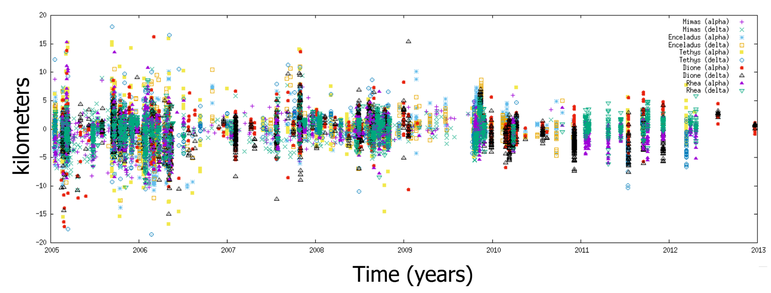
We developed a numerical code that predicts the position of the moons at any time. Then by comparison with the observations, we can correct the value of the physical parameters considered in our model. The precision on the estimated physical quantity is directly related to the precision of the astrometric measurements.

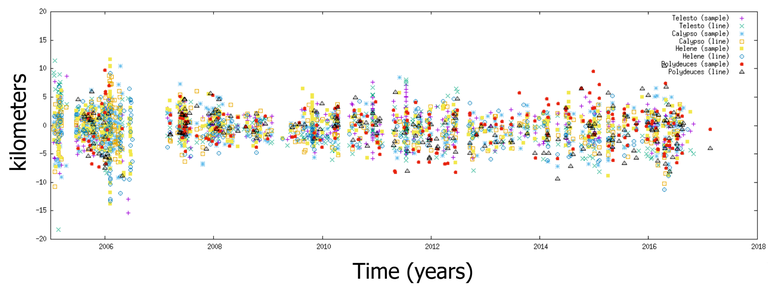
Our code takes into account:

- Mutual perturbations of Saturn and its twenty closest moons
- Extended gravity fields of all objects
- Solar and planetary perturbations
- Precession of Saturn's pole
- Tidal effects inside Saturn and Enceladus
- Physical libration of the inner moons
- General relativity

"Residuals"

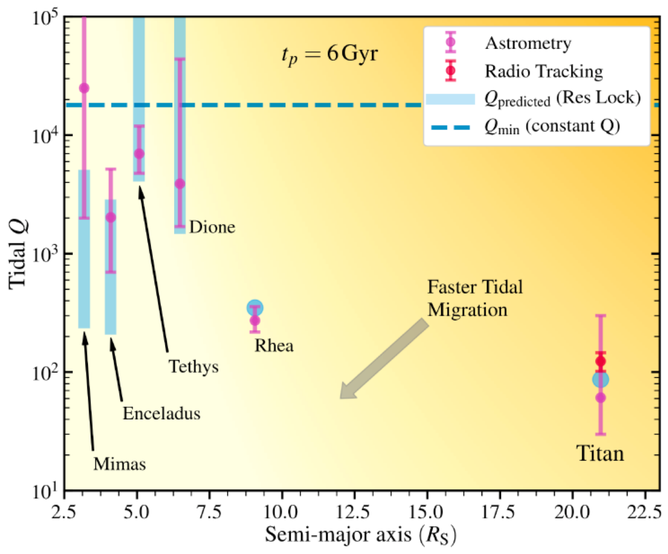
Typical differences between our model and the Cassini-ISS observations:





What we have found…

We found that the inner moons of Saturn are close to homogeneity. More importantly, we have quantified the orbital expansion of six main moons of Saturn!



Unlike commonly believed, we have found that the moon's orbital expansion is barely decreasing with distance. A very non intuitive thing caused by the excitation of waves inside the atmosphere of Saturn.

Believe it or not: The associated physical mechanism was published only three years ago...

What was not expected…

Daphnis is a very small moon evolving at the outer edge of the Saturn's rings. Sounds boring? For a mysterious reason its ephemeris was almost unpredictable within several hundreds of kilometers!

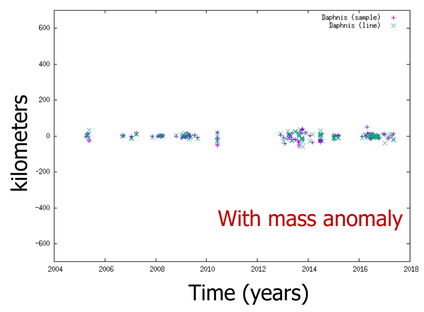


?



3 x Daphnis' period = 4 x Saturn's rotation

A mass anomaly inside Saturn at the proper frequency might create a strong perturbation on Daphnis only.

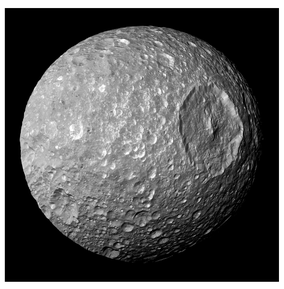


Mimas: A new hope

In 2014, Mimas was found to possess a global ocean under its icy crust or a very elongated silicate core. Both scenarios would imply very different formation and evolution. Unfortunately, it's hard to drill a hole inside Mimas…



?



Global ocean VS. elongated core → **different orbital motion!**

Your take away

- We found that tidal effects in Saturn may rely on a different physical mechanism than previously thought
- Formation and orbital evolution of the main moons have to be reconsidered in light of our results
- Even long-term evolution of Jupiter's system and giant exo-planets should be reconsidered in light of this new tidal paradigm
- Astrometry is like a chocolate box: "you never know what you're gonna get!"

Acknowledgments

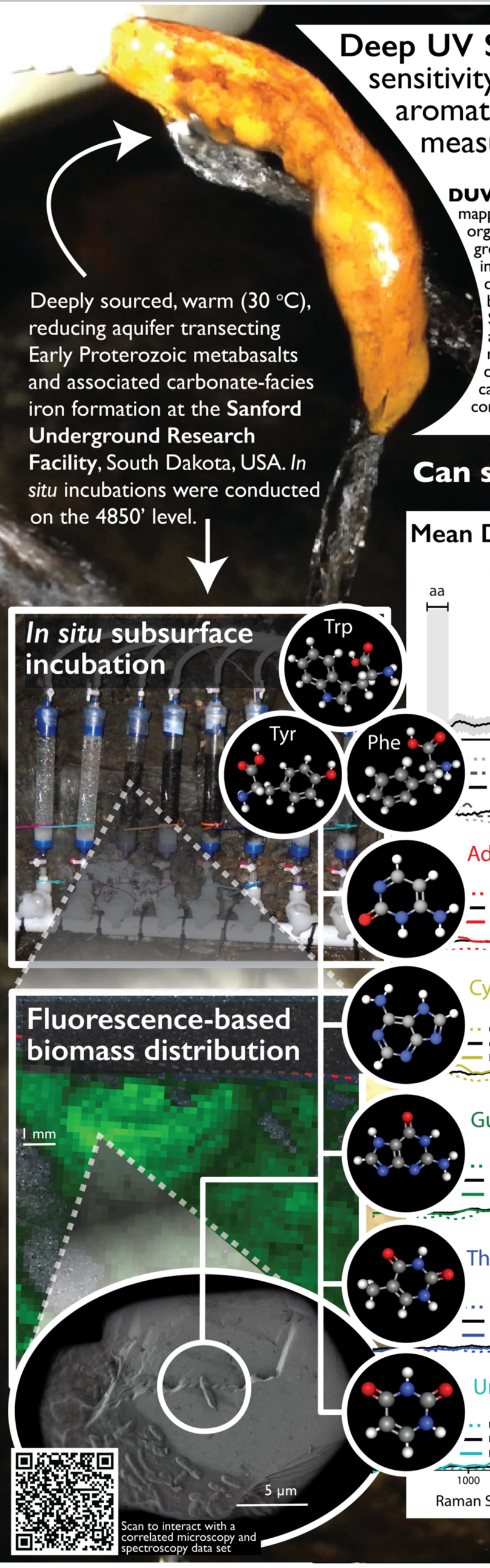
VL's research was supported by an appointment to the NASA Postdoctoral Program at the NASA Jet Propulsion Laboratory, California Institute of Technology, administered by Universities Space Research Association under contract with NASA.

No. P-18

National Aeronautics and Space Administration

Using Deep UV Spectroscopy to Localize Biomass and Define Biosignatures in the Deep Terrestrial Subsurface

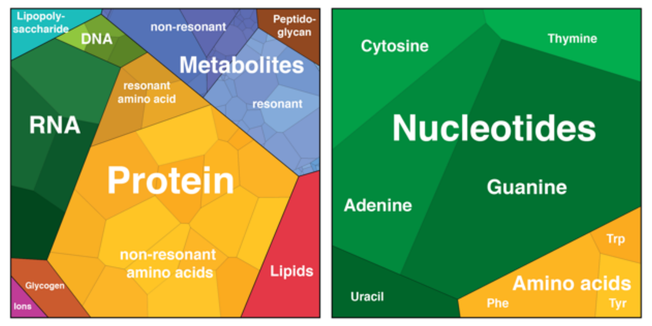
H. M Sapers (3225-affiliate)
J. Razzell Hollis (3225-affiliate), R. Bharita (3225) , L. Beegle (3200), J, Amend (USC), V. J. Orphan (CalTech)



Deeply sourced, warm (30 °C), reducing aquifer transecting Early Proterozoic metabasalts and associated carbonate-facies iron formation at the **Sanford Underground Research Facility**, South Dakota, USA. *In situ* incubations were conducted on the 4850' level.

Deep UV Spectroscopy: excitation with a deep ultra violet (248.6 nm) laser. Increased sensitivity and selectivity due to resonance enhancement of vibrational modes in aromatic organic molecules. Fluorescence-free Raman emission allow for measurements on complex, environmental substrates.

DUV Fluorescence spectroscopy: mapping based on Fluorescence aromatic organic molecules. Below left, shown in green is fluorescence mapping at 320 nm indicating biomass distribution on a rock chip incubated at the 4850' level of SURF based on amino acid fluorescence. Scanning electron microscopy imaging of a high intensity region (inset) shows rod-shaped cells attached to the rock chip. Raman spectroscopy (below right) can then be used to assess molecular components.

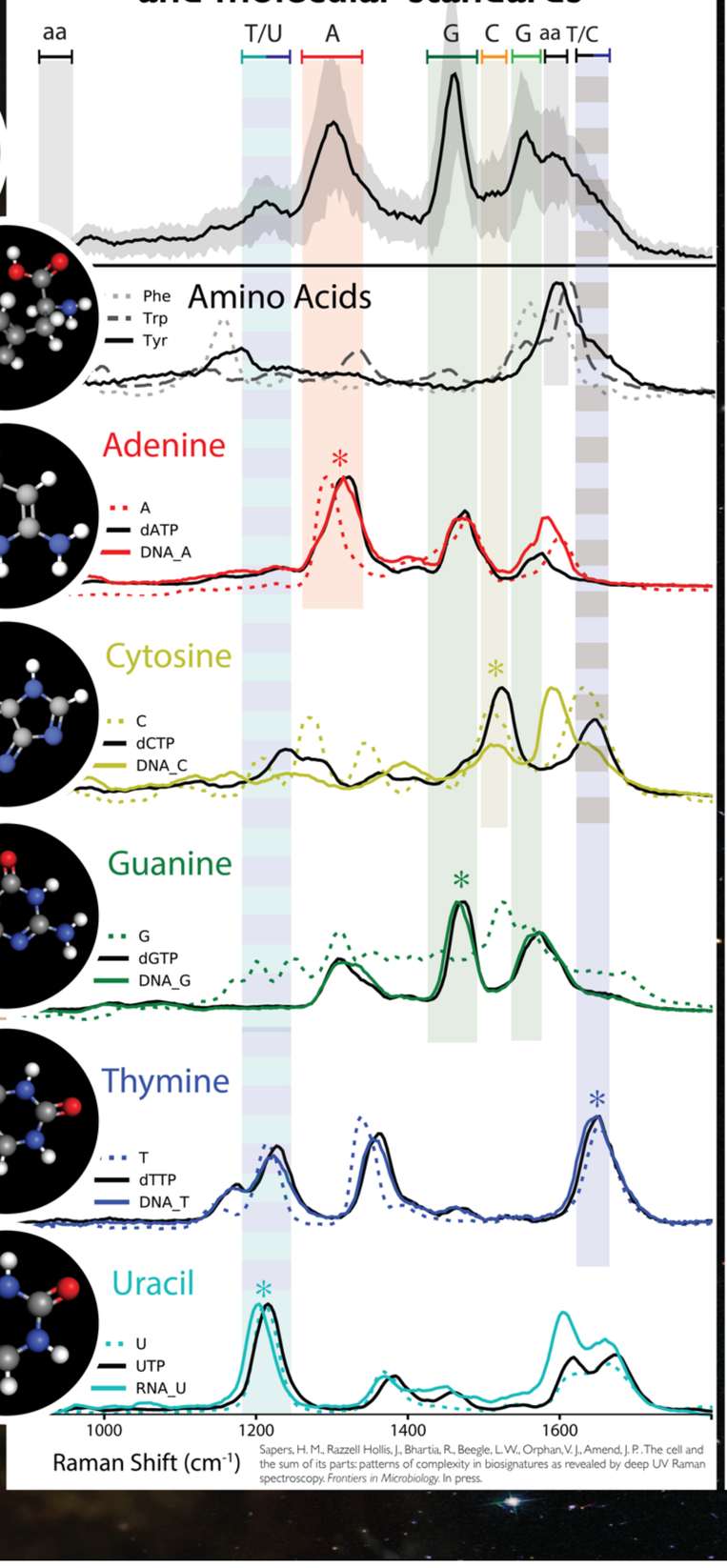


Schematic representation of cell components by dry mass (left), and integrated Raman intensities (right) from deconvolution of the E. coli Raman spectrum using nucleotide and amino acid spectra.

DUV Raman spectroscopy: molecular fingerprinting, complexity and isotopic differentiation of *E coli* cultures. The complexity of a cell can be reduced to a subset of 8 organic molecules (black circles, lower left). The DUV Raman spectrum of a cell is dominated by resonantly enhanced vibrational modes in the nucleobases and aromatic amino acids reflecting a distinct concentration of specific organic molecules. A sufficient molecular complexity of these molecules is required to adequate deconvolute the cellular Raman spectrum (below right)

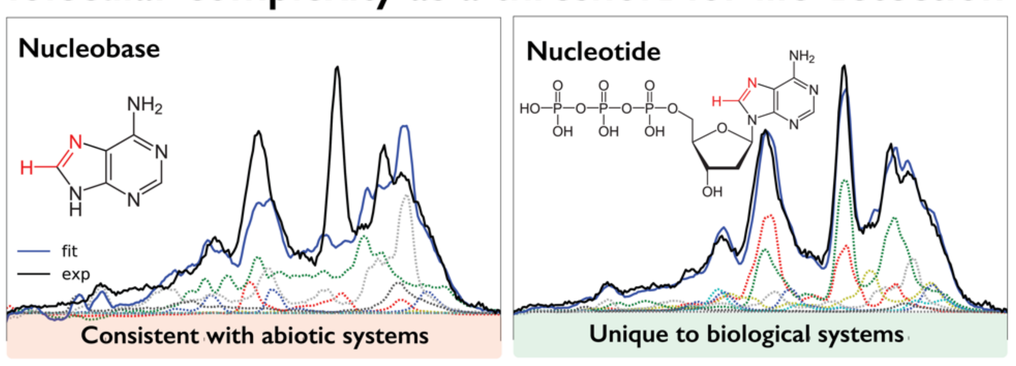
Can spectroscopically detected organics be uniquely attributed to biomass?

Mean DUV Raman spectrum of *E. coli* and molecular standards



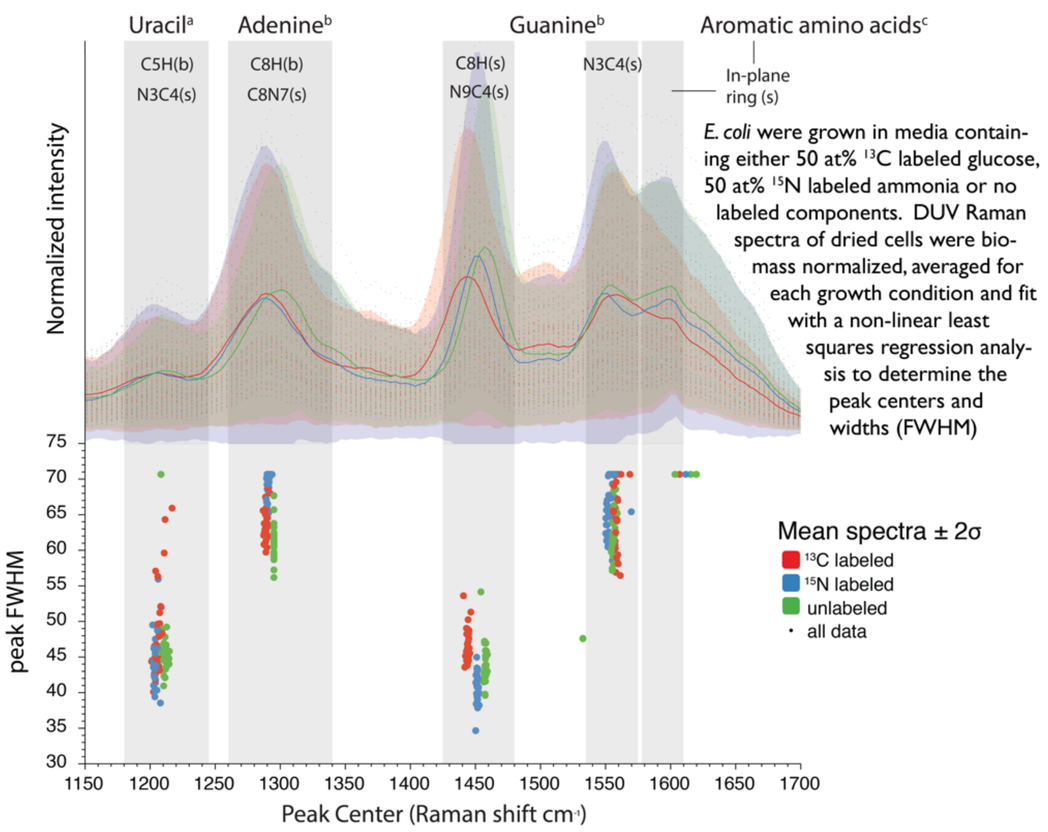
Sapers, H. M., Razzell Hollis, J., Bhartia, R., Beegle, L.W., Orphan, V. J., Amend, J. P.. The cell and the sum of its parts: patterns of complexity in biosignatures as revealed by deep UV Raman spectroscopy. *Frontiers in Microbiology*. In press.

Molecular complexity as a threshold for life detection



Deconvolution based on nucleobases (above L) and nucleotides (above R) illustrates that the DUV Raman spectrum of *E. coli* reflects a molecular complexity unique to life. A linear combination of the DUV resonant compounds (left) is insufficient to fully describe the cellular spectrum It is clear that there are distinctive and measurable spectral features that distinguish a cell from a simple mixture of its most DUV resonant components (Sapers et al, in press).

DUV Raman can differentiate cells labeled with stable isotope probing



E. coli were grown in media containing either 50 at% ^{13}C labeled glucose, 50 at% ^{15}N labeled ammonia or no labeled components. DUV Raman spectra of dried cells were biomass normalized, averaged for each growth condition and fit with a non-linear least squares regression analysis to determine the peak centers and widths (FWHM)

Culture-based studies indicate that DUV Raman can be used to reliably differentiate bacterial cells labeled with ^{13}C or ^{15}N based on both distinctive red-shifting and broadening of characteristic Raman peaks. Red-shifting results as increasing the mass of an oscillating atom in a resonantly enhanced vibration will result in Raman emission at longer wavelength and therefore a smaller Raman shift. Peak broadening occurs as labeling introduces isotopologues and the Raman peaks represent a larger population of vibrations. Identifying labeled bacteria shows promise for DUV Raman-SIP on environmental substrates in natural systems (Sapers et al., in prep).

National Aeronautics and Space Administration
Jet Propulsion Laboratory
California Institute of Technology
Pasadena, California

www.nasa.gov

Poster No. P-19

Copyright 2019. All rights reserved.

Changes in Surface Dust Coverage using Mars Climate Sounder

Author: Jonathan Bapst (3222)
Sylvain Piqueux (3222)

Outstanding Question(s)

1. **Does surface dust move globally?**
2. **Where are the sources and sinks?**
3. **What are the net fluxes?**

Motivation

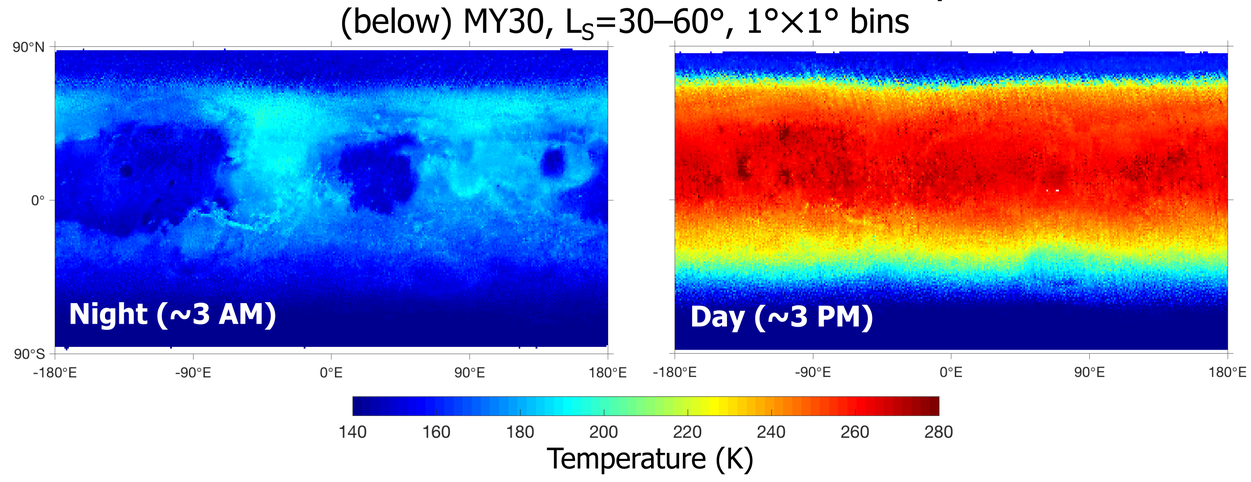
- Dust cycle is important part of Mars' climate system
- Large dust storms are thought to redistribute substantial volumes of dust, however this remains unquantified
- Understanding the climate is important for interpreting geology, evaluating habitability, and surface mission operations

Methods

- Use atmospherically-corrected surface temperatures from Mars Climate Sounder (MCS) and a thermal model, KRC, to constrain physical properties and albedo
- Identify systematic interannual changes and avoid seasonal effects by comparing seasonal slices of 30° L_S

5+ Mars Years of MCS Global Surface Temperatures

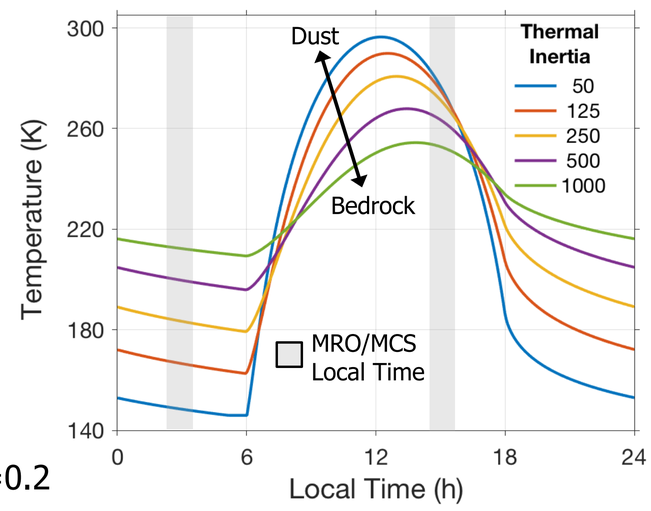
(below) MY30, L_S=30–60°, 1°×1° bins



Deriving Thermal Inertia and Surface Albedo

- Best-fit model to AM **and** PM MCS surface temperatures
  - Thermal inertia is better constrained by nighttime temperatures
  - Albedo is better constrained by daytime temperatures

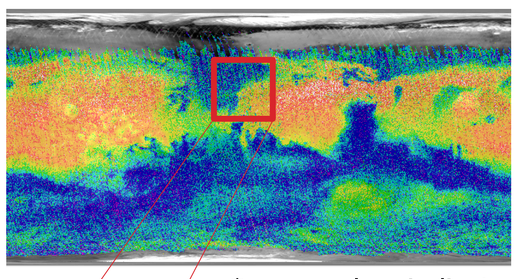
(right) Equatorial models, L_S=0°, albedo=0.2



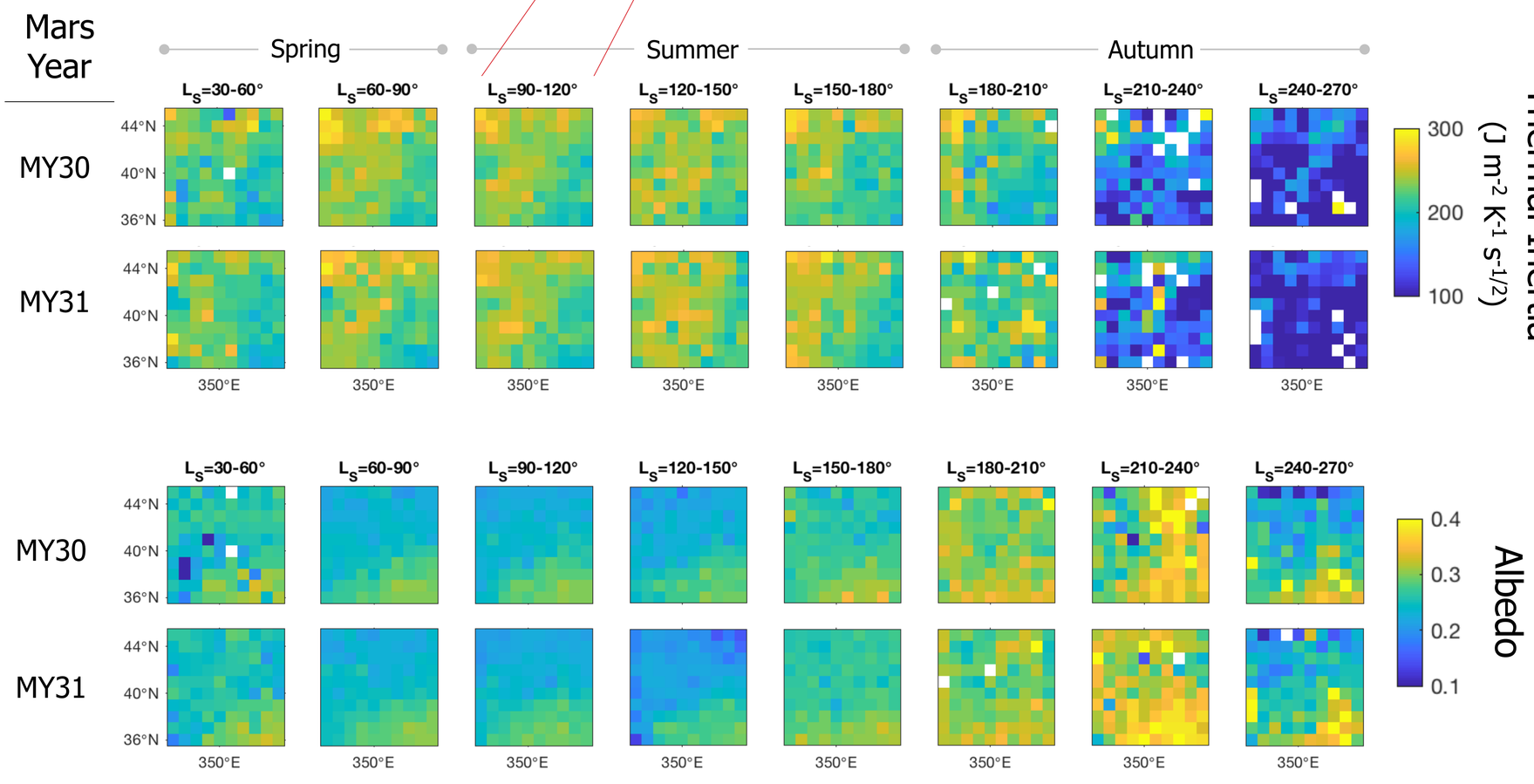
First Results

- Preliminary runs: 10°×10° region of Acidalia for MY30 and MY31
- No evidence for interannual change

Global Dust Index

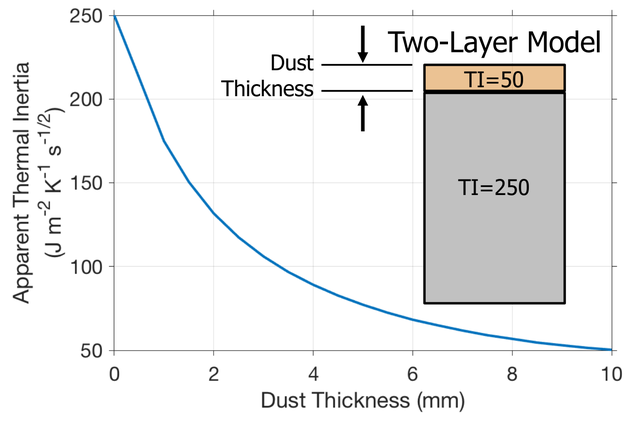


*warm colors indicate dusty regions



Next Steps

- Analyze **global** data for systematic interannual changes
- Filter out atmospheric effects
- Quantify changes in dust thickness from changes in thermal inertia (see below) and surface albedo



National Aeroautics and Space Administration
Jet Propulsion Lanboratory
California Institute of Technology
Pasadena, California

www.nasa.gov

Copyright 2019. All rights reserved.

Poster No. P-20

National Aeronautics and Space Administration

Surface Alteration from Landing InSight on Mars and its Implications for Shallow Regolith Structure

N. R. Williams (3223) and M. P. Golombek (3223)

Introduction

- InSight used retropropulsive rockets to land at Homestead hollow in Elysium Planitia on Mars on Nov. 26, 2018, at 4.502384°N, 135.623447°E[1-3].
- Rocket exhaust modifies the near surface by redistributing primarily fine-grained materials[4-8].
- Most easily identified as “halos” of albedo, color, and/or textural variations, removal of bright dust[4-7] or changes in surface roughness[8].
- InSight’s surface alteration can be compared to other landing sites as well as impacts to assess surface properties and structure of the upper regolith.

Methodology

- High Resolution Imaging Science Experiment (HiRISE)[9] acquired ~25 cm/pixel infrared/red/blue (IRB) color images on Dec. 6 & 11, 2018 (Fig. 1).
- Diffuse halo boundaries were difficult to define, so we performed a decorrelation stretch (DCS) -- a principal component analysis that enhances color in a multispectral image with significant band-to-band correlation.

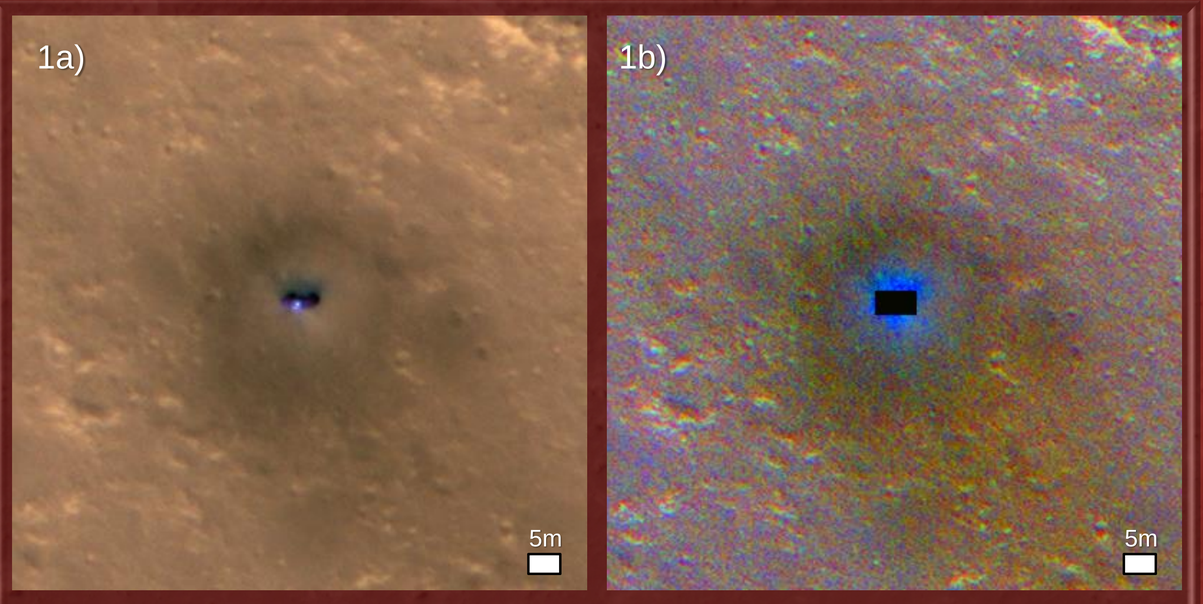


Fig. 1: a) False-color (IRB) stretch of HiRISE image ESP_057939_1845 over the InSight landing site, and b) decorrelation stretch of the image (excluding lander itself in black rectangle) to enhance surface spectral differences

- InSight’s Instrument Deployment Camera (IDC) also acquired red/green/blue (RGB) color images [10] of the terrain around the lander on sol 14 / Dec. 11, 2018 (Fig. 2)[1].
- DCS stretch was performed on IDC RGB mosaic as well, although lighting artifacts across image seams become more apparent (Fig. 2).

Results

- Low-reflectance outer halo extends 15-21 m (~990 m^2 area) from the lander with a 35% lower relative albedo than unaltered background, and extends southeast along the expected prevailing wind direction[11].
- Inner halo extends 8-11 m with an 18% lower albedo than unaltered background.
- Discontinuous pattern of low-reflectance rays (showing up as dark-blue in Fig. 1a) extends primarily towards the north up to 5 m from the lander.
- HiRISE IRB DCS and IDC RGB panorama DCS and color ratios show inner halo is disproportionately brighter at short visible wavelengths (green or blue) in contrast with the more distal unaltered background terrain (brighter red).

Interpretations/Conclusions

- InSight’s outer halo extending 15-21 m (~990 m^2 area) is very similar to Phoenix’s (same lander system) with an 18 m mean radius (1020 m^2)[7].
- Darkening by 35% is consistent with removal of a thin layer (μm) of dust similar to previous Mars landing sites[4-7] including ~20-40% by Phoenix[5], an average 35% by fresh impacts[6], and analogous to dust devil tracks[12].
- Previous Mars landings did not produce high-reflectance halos, but impacts sometimes expose bright materials[6].
- IDC images 1-2 m south of the lander show radial grooves and ridges suggesting a scour from landing removed some unconsolidated regolith and exposed underlying material[13-15].
- Rockets also excavated steep-sided pits under the lander (Fig. 3) suggesting a mildly cohesive duricrust[15], which may be partially exposed as the high-reflectance inner halo.



Fig. 3: IDC image (stretched) taken sol 12 showing the pits excavated during landing.

References

[1] Golombek M. P. *et* al. (2019) 50th LPSC, #1694. [2] Parker T. *et al*. (2019) 50th LPSC, #1948. [3] Golombek M. P. *et al*. (2017) Space Sci. Rev. 211, 5-95. [4] Johnson J. R. *et al*. (2014) Icarus 249, 74-92. [5] Daubar I. J. *et al*. (2015) 46th LPSC, #2225. [6] Daubar I. J. *et al*. (2016) Icarus 267, 86-105. [7] Lorenz R. D. (2016) Planet. Space Sci. 127, 91-94. [8] Clegg R. N. *et al.* (2014) Icarus 227, 176-194. [9] McEwen A. S. *et al*. (2007) JGR 112, E5. [10] Maki J. N. *et al*. (2018) Space Sci. Rev. 214, 105. [11] Golombek M. P. *et al*. (2018) Space Sci. Rev. 214, 84. [12] Reiss D. and Lorenz R. D. (2016) Icarus 266, 315-330. [13] Grant J. A. *et al*. (2019) 50th LPSC, #1199. [14] Weitz C. M. *et al*. (2019) 50th LPSC, #1392. [15] Ansan V. *et al*. (2019) 50th LPSC, #1310. [16] E. Hauber *et al*. (2019) EPSC-DPS, #1794.

Fig. 2: a) InSight sol 14 IDC panorama of the landing site, and b) decorrelation stretch (with sky and lander masked out from analysis) to enhance surface spectral differences. White arrows indicate apparent extent of alteration zone.

National Aeronautics and Space Administration

Jet Propulsion Laboratory
California Institute of Technology
Pasadena, California

www.nasa.gov

Copyright 2019. All rights reserved.

Poster No. P-21